LATE PALEOZOIC–EARLY MESOZOIC GRANITOIDS IN THE KHANGAY–KHENTEY BASIN, CENTRAL MONGOLIA: IMPLICATION FOR THE TECTONIC EVOLUTION OF THE MONGOL–OKHOTSK OCEAN MARGIN

Ariuntsetseg Ganbat [1,2,*] **ariun.0602@gmail.com**

Tatsuki Tsujimori [1,3] **tatsukix@tohoku.ac.jp**

Laicheng Miao [4] **miaolc@mail.iggcas.ac.cn**

Inna Safonova [5,6] **inna03-64@mail.ru**

Daniel Pastor-Galán [1,3,7] **dpastorgalan@gmail.com**

Chimedtseren Anaad [2,9] **chimedtserena@yahoo.com**

Munkhtsengel Baatar [2,8] **tsengel@must.edu.mn**

Shogo Aoki [10,11] **s-aoki@gipc.akita-u.ac.jp**

Kazumasa Aoki [11] **kazumasa@das.ous.ac.jp**

Ilya Savinskiy [5] **ilya.savinskiy@gmail.com**

[1] Department of Earth Science, Graduate School of Science, Tohoku University, Aoba, Sendai 980-8578, Japan

[2] Geoscience Center, Mongolian University of Science and Technology, Ulaanbaatar 120646, Mongolia

[3] Center for Northeast Asian Studies, Tohoku University, Aoba, Sendai 980-8576, Japan

[4] Institute of Geology and Geophysics, Chinese Academy of Sciences, Beijing 100029, China

[5] Novosibirsk State University, Pirogova St. 1, Novosibirsk, 630090, Russia

[6] Sobolev Institute of Geology and Mineralogy, SB RAS, Koptyuga ave. 3, Novosibirsk, 630090, Russia

[7] Frontier Research Institute for Interdisciplinary Sciences, Tohoku University, Aoba, Sendai 980- 0845, Japan

[8] Mongolian University of Science and Technology, Ulaanbaatar 120646, Mongolia

[9] Natural History Museum of Mongolia, Ulaanbaatar, 120646, Mongolia

[10] Graduate School of International Resource Sciences, Akita University, Akita 010-8502, Japan

[11] Center for Fundamental Education, Okayama University of Science, Okayama 700-0005, Japan

---

This Manuscript has been submitted for publication in LITHOS in April, 2021. Please note that despite having undergone peer-review, the manuscript has not been formally accepted yet for publication and, therefore, it may be subject to some changes. Subsequent versions of the manuscript may include slightly different content. If accepted the final version of the manuscript will be available through the “PEER REVIEW PUBLICATION DOI” link.

Late Paleozoic–Early Mesozoic granitoids in the Khangay–Khentey basin, Central Mongolia: Implication for the tectonic evolution of the Mongol–Okhotsk Ocean margin

Ariuntsetseg Ganbat [1,2,*] https://orcid.org/ 0000-0003-2464-4161
Tatsuki Tsujimori [1,3] https://orcid.org/0000-0001-9202-7312
Laicheng Miao [4] https://orcid.org/ 0000-0001-6296-4444
Inna Safonova [5,6] https://orcid.org/ 0000-0003-2464-4161
Daniel Pastor-Galán[1,3,7] https://orcid.org/ 0000-0002-0226-2739
Chimedtseren Anaad [2,9] https://orcid.org/ 0000-0001-7878-0738
Munkhtsengel Baatar [2,8] https://orcid.org/ 0000-0002-9644-3599
Shogo Aoki [10,11] https://orcid.org/ 0000-0001-5093-1346
Kazumasa Aoki[11] https://orcid.org/ 0000-0001-7645-6766
Ilya Savinskiy [5] https://orcid.org/ 0000-0001-9430-9794

[1] Department of Earth Science, Graduate School of Science, Tohoku University, Aoba, Sendai 980-8578, Japan
[2] Geoscience Center, Mongolian University of Science and Technology, Ulaanbaatar 120646, Mongolia
[3] Center for Northeast Asian Studies, Tohoku University, Aoba, Sendai 980-8576, Japan
[4] Institute of Geology and Geophysics, Chinese Academy of Sciences, Beijing 100029, China
[5] Novosibirsk State University, Pirogova St. 1, Novosibirsk, 630090, Russia
[6] Sobolev Institute of Geology and Mineralogy, SB RAS, Koptyuga ave. 3, Novosibirsk, 630090, Russia
[7] Frontier Research Institute for Interdisciplinary Sciences, Tohoku University, Aoba, Sendai 980-0845, Japan
[8] Mongolian University of Science and Technology, Ulaanbaatar 120646, Mongolia
[9] Natural History Museum of Mongolia, Ulaanbaatar, 120646, Mongolia
[10] Graduate School of International Resource Sciences, Akita University, Akita 010-8502, Japan
[11] Center for Fundamental Education, Okayama University of Science, Okayama 700-0005, Japan

1. Introduction

The continental crust of the Earth is unique by the presence of granites, compared to other planets of the solar system. Its origin and evolution have been a matter of debate among Earth scientists for a long time (Taylor and McLennan, 1995; Chen and Grapes, 2007). Granites are essential for deciphering crustal growth and tectonic evolution of the Earth and for assessing related mineral deposits (e.g., Clemens et al., 2020). Granites and their associated volcano-plutonic suites can provide critical information about orogeny-related igneous petrogenesis and geodynamic framework. Petrogenetic and tectonic reconstructions require zircon U-Pb age dating and up-to-date geochemical and isotopic studies (e.g., Pearce and Peate, 1995; Kemp et al., 2006). The Central Asian Orogenic Belt (Fig. 1a; CAOB or Altaids) is the world largest accretionary orogenic belt separating the Siberian, Kazakhstan, Tarim, and North China continental blocks and is the site of the most significant Phanerozoic juvenile crustal growth on Earth (e.g., Jahn et al., 2004; Windley et al., 2007; Xiao et al., 2010; Safonova et al., 2011, 2017; Kröner et al., 2014). Evidence for the dominantly juvenile character of the CAOB crust comes from low whole-rock initial Sr and high Nd and high Hf-in-zircon isotopic values of the CAOB igneous rocks and from the Pacific-type nature of the CAOB constituting local orogenic belts (e.g., Jahn et al., 2004; Safonova et al., 2011, 2017; Wilhem et al., 2012). However, the proportions of juvenile and recycled crust in the CAOB, hosting numerous volcano-plutonic complexes/suites (Fig. 1b), are still a matter of debates as many formations still lack up-to-date analytical data and many areas lack reliable tectonic models (e.g., Jahn et al., 2004; Kröner et al., 2014; Safonova, 2017). The solution to these problems requires reconstructing tectonic frameworks in different segments of the CAOB.

The CAOB was formed by the evolution and suturing of the Paleo-Asian Ocean and its related oceanic realms or branches, e.g., Turkestan or South Tienshan Ocean in the west and Mongol–Okhotsk Ocean (MOO) in the east. The closure of the MOO by the approaching Siberian and Central Mongolia–Erguna block in the Late Paleozoic–Mesozoic time led to the formation of the Mongol–Okhotsk Belt (MOB) in the northeastern CAOB (e.g., Donskaya et al., 2013; Yi and Meert, 2020). The MOB hosting numerous volcano-plutonic series is the youngest and one of the most critical segments of the CAOB and hosts numerous volcano-plutonic series (Fig. 1b). Despite the extensive research during the last three decades, whether these volcano-plutonic series are related to the evolution of the MOO is still an issue of hot debate. One viewpoint is that they have been formed in a within plate setting without any link with the MOO (Yarmolyuk et al., 2002). An alternative model is that they were related to the subduction of MOO. Another uncertainty is whether this ocean closed with bi-directional subduction (Tomurtogoo et al., 2005) or whether there was subduction along the northern margin beneath the Siberian craton (e.g., Munkhtsengel et al., 2007; Donskaya et al., 2013), or southern margin beneath the Central Mongolia–Erguna Block which is also referred to as Amur or Amurian Superterrane (e.g., Zhu et al., 2016; Zhao et al., 2017; Sorokin et al., 2020).

It needs to point out that previous studies of the MOB were mostly within the territories of China (e.g., Sun et al., 2013; Liu et al., 2018) and Russia (e.g., Izbrodin et al., 2020). The amount of up-to-date geochronological and geochemical data from granitic plutons and volcano-plutonic belts in the Mongolian part of the belt remains limited to solve confidently the problem of their origin and subduction evolution of the MOO. In this paper, we present U-Pb zircon ages, major and trace element geochemical data, whole-rock Nd and in-situ zircon Hf isotopic compositions for the granitic plutons hosted by the Khangay and Khentey Batholiths (Figs. 1b, 1c), in an attempt to constrain the formation time of the granitic plutons or the volcano-plutonic series, to understand their petrogenesis, and to reconstruct geodynamic settings of their formation. The new results will shed light on the Late Paleozoic–Early Mesozoic evolution of the MOB, as well as the nature of continental crust growth in the eastern CAOB.

2. Regional and local geology

The territory of Mongolia occupies a central position within the CAOB (Fig. 1b), and has been subdivided into two tectonic domains by the Main Mongolian Lineament (MML), to the northern and the southern (Badarch et al., 2002; Tomurtogoo et al., 2005). The northern domain comprises cratonic fragments, Neoproterozoic ophiolites, Precambrian and Early Paleozoic metamorphic rocks, and Early Paleozoic basins with clastic rock, island arcs, and associated volcanoclastic sediments (Badarch et al., 2002). The southern domain consists of Paleozoic island arcs, ophiolite fragments, and Late Carboniferous to Permian volcanic rocks (Wilhem et al., 2012). These two domains are bounded by Khangay–Khentey basin, part of the Mongol–Okhotsk Belt.

The Mongol–Okhotsk Belt extends over a distance of more than 3,000 km from Central Mongolia to the Uda Bay in the Okhotsk Sea over the territories of Mongolia, Russia, and NE China (Fig. 1b). The Silurian to Carboniferous oceanic sedimentary sequences of the Khangay–Khentey basin (part of the Mongol–Okhotsk Belt) are overlain by Triassic terrigenous continental deposits. The Khangay–Khentey basin also includes the Adaatsag and Khuhu Davaa ophiolites with crystallization ages from 314 to 325 Ma, and associated accretionary complexes (Tomurtogoo et al., 2005; Zhu et al., 2018) marking the suture zone of the MOO (Fig. 2). The accretionary complexes include oceanic basalt (mostly OIB-type), Silurian–Devonian radiolarian pelagic chert, hemipelagic siliceous mudstone and siltstone, and trench turbidite, all elements of Ocean Plate Stratigraphy (OPS), and fore-arc greywacke sandstone (e.g., Dagva-Ochir et al., 2020). The U-Pb ages of detrital zircons show that the sedimentary records of the Khangay–Khentey basin were started after Early

Carboniferous time (Badarch et al., 2002; Bussien et al., 2011). The general geology and the numerous intrusions of mafic to felsic igneous rocks younging from west to east along the Mongol–Okhotsk suture (Donskaya et al., 2013), suggest that the ocean closed in a scissor-like manner during a period from the late Carboniferous to the Permian in central Mongolia and/or until the Triassic–Early Jurassic or Cretaceous in southeastern Transbaikalia and NE China, but the accurate time of its closure remains debatable (e.g., Sorokin et al., 2020). The subduction of the MOO can be responsible for the paired volcano-plutonic belts that once existed around the suture, hosting abundant granitoid intrusions: plutons with various sizes and huge batholiths. Among those are Angara-Vitim, Erguna, Khangay, and Khentey Batholiths (Fig. 1b). The Angara-Vitim batholith developed on the heterogeneous basement as its granitoids yielded U-Pb ages ranging from 278 to 333 Ma (e.g., Izbrodin et al., 2020). The Erguna batholith formed in an arc and back-arc settings in Carboniferous time (e.g., Sun et al., 2013), and continued until Early–Middle Jurassic (Liu et al., 2018). The Khangay Batholith is located in the western Mongol–Okhotsk Belt (Fig. 1c). It consists of several plutonic complexes formed in two stages. The earlier intrusion of granodiorite, tonalite, plagiogranite, and gabbro-diorite was followed by the intrusion of diverse granitoids, such as hornblende biotite granite, biotite-tonalite, granodiorite, and alkaline granite. The available U-Pb zircon, Rb-Sr isochron, and Ar/Ar ages from the Khangay batholith range from 237 to 263 Ma (Jahn et al., 2004). The Khentey batholith is dominated by granodiorite and leucogranite with subordinate gabbro and diorite. The U-Pb zircon ages and Rb-Sr isochron ages obtained from Khentey granitoids range from 186 to 226 Ma (Yarmolyuk et al., 2002). To the south, the Khentey batholith is bordered by abundant coeval series of bimodal volcanic rocks and alkaline Li-F granites (e.g., Yarmolyuk et al., 2002).

Of special interest is the Selenge volcano-plutonic Belt located in the northern MOB (Fig. 1c) as it hosts the world-famous Erdenet copper-porphyry deposit. The Selenge Pluton which is closely related to the mineralization is a composite intrusion. The oldest Selenge Pluton (253–277 Ma) consists of calc-alkaline shoshonite-latite rocks, and coeval volcanics (Munkhtsengel et al., 2007). The younger 240 Ma quartz-diorite yielded $\varepsilon_{Hf}(t)$ values from + 6.9 to + 14.8 and T_{DM2} (Hf) ages between 320 and 830 Ma. The Triassic magmatic activity formed alkaline intrusions and bimodal igneous series different from older subduction-related magmas (Morozumi et al., 2003). The ore-bearing Erdenet intrusions yielded an age of 235–245 Ma and molybdenite yielded a Re–Os age of 240 Ma (Morozumi et al., 2003).

The study area is located in the southern margin of the Khangay–Khentey basin, northwest of the Mongol–Okhotsk suture near the Delgerkhaan town (Fig. 2). It hosts several granitoid plutons, including undifferentiated bodies and namely Batkhaan, Zambalkhudag, Delgerkhaan plutons, which are foci of this paper. They are compositionally caries from diorite, granodiorite, minor monzogranite to alkaline granite (Tumurchudur et al., 2006). The Batkhaan granitoid pluton of Permian age consists of subalkaline granite, syenogranite, quartz syenite, quartz diorite, associated with trachyrhyolite, rhyolite, and dacite. This association is overlain by Late Permian conglomerate, silicified sandstone, and siltstone strata with fauna and flora. The Delgerkhaan granitoid pluton occupies a large area and consists of calc-alkaline biotite-hornblende granite, granodiorite, monzodiorite, monzogabbro carrying mafic xenoliths (Tumurchudur et al., 2006; Amar-Amgalan, 2008). The Delgerkhaan granitoids are cut by numerous NE-trending 1–3 m wide mafic to intermediate dykes. Near the granitoid body, there are outcrops of mafic to felsic volcanic rocks. Biotite from trachyandesite yielded a K-Ar age of 223 Ma (Tumurchudur et al., 2006). According to the 1:200 000 scale State Geological Map (Dagvadorj et al., 1993), the Zambalkhudag pluton consists of Late Carboniferous calc-alkaline biotite- granite, granodiorite, and leucogranite. An undifferentiated smaller body, previously assumed as Cambrian granite-granodiorite, is overlain by felsic volcanogenic formations, which lithostratigraphic age is accepted as Early Permian (Fig. 2) (Dagvadorj et al., 1993). The igneous rocks intrude Devonian–Carboniferous dark gray sandstone, polymictic sandstone, conglomerate, gravel, and chert. In addition, there are Late Triassic syenite, diorite, monzodiorite, and mafic to intermediate volcanic rocks and Cretaceous basaltic andesite all covered by oil-bearing shale-siltstone-sandstone strata (Tumurchudur et al., 2006).

3. Analytical methods

3.1 Zircon U-Pb geochronology

Zircon crystals were separated in Tohoku University, using standard techniques including conventional rock-crushing, magnetic and heavy liquid separation, and handpicking under a binocular microscope. Then, zircon crystals were mounted in epoxy discs. Zonation of zircon interiors was documented using cathodoluminescence (CL) imaging using a Hitachi S-3400N scanning electron microscope, equipped with a Gatan MiniCL. In-situ zircon U-Pb dating was carried out in the Okayama University of Science by using a Thermo Fisher Scientific iCAP-RQ single-collector quadrupole coupled to a Teledyne Cetac Technologies Analyte G2 ArF excimer laser ablation (LA) system equipped with a HelEx 2 volume sample chamber. The laser ablation was conducted at the laser spot size of 25 µm, the fluence of 1.8 J/cm^{2,} and the repetition rate of 5 Hz (for details see Aoki et al., 2020). Zircon standard 91500 (1065 Ma; Wiedenbeck et al., 2004) was used for age calibration, NIST SRM 612 standard (Jochum et al., 2011) for instrument optimization, and Plešovice zircons (337 Ma; Sláma et al., 2008) as secondary standards for quality control. Zircons from samples D0815 and D0817 were analyzed for U-Pb ages at the Beijing SHRIMP Center, China, with a SHRIMP II, following the standard procedures described in (Jian et al., 2012). Prior to each analysis, the rastering of primary beams, was applied to minimize contamination by surface Pb. Standards M257 (561.3 Ma, U = 840 μg/g; Nasdala et al., 2008) and TEMORA (417 Ma; Black et al., 2003) were used for the calibration of U concentrations and U-Pb ages, respectively. U-Pb ages and concordia diagrams were calculated and plotted using IsoplotR software (ver. 3.75; Vermeesch, 2018); the concordia age of each sample incorporates errors on decay constants and includes evaluation of the concordance of apparent ages. The concordia ages and errors are presented at the two-sigma level.

3.2 Whole-rock geochemistry

Twenty-five samples were selected for whole-rock analysis. Concentrations of major and trace elements were measured at Activation Laboratories Ltd., Canada, using Code 4Litho Lithogeochemistry Package with fusion inductively coupled plasma optical emission spectrometry (FUS-ICPOES) and inductively coupled plasma mass spectroscopy (FUS-ICPMS), respectively. Thirty-one more samples were analyzed at the Key Laboratory of Lithospheric Evolution, Institute of Geology and Geophysics CAS. Major oxides were obtained from X-ray fluorescence (XRF) with the analytical uncertainties ranging between 1–3%. An Inductively Coupled Plasma Mass Spectrometer (ICP-MS) was used to determine rare earth elements (REE) and trace elements. The measurement error and drift were controlled by regular analysis of standard samples with a periodicity of 10%. The analyzed uncertainties of ICP-MS data at the μg/g level are better than 3–10% for the trace elements, and ~5–10% for the REE procedure at the Institute of Geology and Geophysics, Chinese Academy of Sciences. Procedural blanks were <100 pg for Sm and Nd. Five more samples of granitoids were analyzed at the Analytical Center for Multi-Element and Isotope Studies of the Institute of Geology and Mineralogy, Novosibirsk, Russia. Major oxides were determined by the X-ray fluorescence (XRF) method using an Applied Research Laboratories ARL-9900-XP analyzer, following the standard procedure. Trace elements were analyzed by mass spectrometry with inductively coupled plasma (ICP-MS) after fusion with $LiBO_2$. Simultaneous determination of all elements was carried out to low, medium, and high resolution, on a Finnigan Element-II high-resolution mass spectrometer with external calibration using BHVO-1 reference samples and an internal standard. The method has been validated through the analysis of nine reference materials. Relative standard deviations for all elements were <10% within the determined concentration ranges.

3.3 Hf-in-zircon isotopes

Hf isotope analyses were carried out using a Neptune Plus MC-ICP-MS (Thermo Fisher Scientific, Germany) in combination with a Geolas 2005 excimer ArF laser ablation system (193 nm) at the Institute of Geology and Geophysics, Chinese Academy of Science, Beijing. The analyses for zircon grains from the granites were conducted with a beam diameter of 63 μm, 6 Hz repetition rate, and energy of 15 mJ/cm^2. This setting yielded a signal intensity of 10 V at 180 Hf for the standard zircon 91500. Typical ablation time was 26 s, resulting in pits 20–30 μm deep. The initial ^{176}Hf/^{177}Hf ratios for the unknown samples were calculated to their initial value, using the measured ^{176}Lu/^{177}Hf ratios, the apparent age of each zircon grain, and a ^{176}Lu decay constant of 1.867×10^{-11} yr^{-1} (Söderlund et al., 2004). The calculations of epsilon Hf were done using a present-day chondritic ^{176}Hf/^{177}Hf value of 0.282785 and ^{176}Lu/^{177}Hf of 0.0336 (Bouvier et al., 2008) and the present-day felsic crustal ratio of ^{176}Lu/^{177}Hf = 0.015.

3.4. Sm-Nd isotopic analysis

Sm-Nd isotopic analyses were performed at the Institute of Geology and Geochronology, Russian Academy of Sciences, Saint-Petersburg. About 100 mg of whole-rock powder was dissolved in a mixture of HF, HNO_3, and $HClO_4$. A ^{149}Sm-^{150}Nd spike solution was added to all samples before dissolution. REEs were separated on BioRad AGW50-X8 200–400 mesh resin using conventional cation-exchange techniques. Sm and Nd were separated by extraction chromatography with a LN-Spec (100–150 mesh) resin. The total blank in the laboratory was 0.1–0.2 ng for Sm and 0.1–0.5 ng for Nd. Isotopic compositions of Sm and Nd were determined on a TRITON TI multi-collector mass-spectrometer. The precision (2σ) of Sm and Nd contents and ^{147}Sm/^{144}Nd ratios were 0.5% and 0.005% for ^{143}Nd/^{144}Nd ratios. ^{143}Nd/^{144}Nd ratios were adjusted relative to a value of 0.512115 for the JNdi-1standard. During the period of analysis, the weighted average of 10 JNdi-1 Nd standard runs yielded 0.512108 ± 7 (2σ) for ^{143}Nd/^{144}Nd, normalized against ^{146}Nd/^{144}Nd = 0.7219. The $\varepsilon_{Nd}(t)$ values were calculated using the present-day values for a chondritic uniform reservoir (CHUR) ^{143}Nd/^{144}Nd = 0.512638 and ^{147}Sm/^{144}Nd = 0.1967 (Jacobsen and Wasserburg, 1984). Whole-rock Nd model ages $T_{Nd(DM)}$ were calculated using the model of Goldstein and Jacobsen (1988) according to which the Nd isotopic composition of the depleted mantle evolved linearly since 4.56 Ga ago and has a present-day value εNd(0) of + 10 (^{143}Nd/^{144}Nd =0.513151 and ^{147}Sm/^{144}Nd = 0.21365). Two-stage (crustal) Nd model ages $T_{Nd(C)}$ were calculated using a mean crustal ratio ^{147}Sm/^{144}Nd of 0.12.

4. Results

4.1 Petrography

The most abundant igneous rock types in the study area are granite, granodiorite, syenogranite, quartz monzonite andesite, and trachyandesite (Fig. 3). Mineral assemblages of representative samples are given in Table 1. The major constituent minerals in undifferentiated granodiorite (sample D0925) are plagioclase (~44%), quartz (~25%), K-feldspar (~25%) (Fig. 3a). The accessory minerals are magnetite, apatite, and zircon (~1%). Batkhaan inequigranular syenogranite (sample D1710) possesses hypidiomorphic texture with myrmekite intergrowths (Fig. 3b). Major minerals are anhedral quartz (~40%), euhedral to subhedral perthitic K-feldspar (phenocrysts of microcline or orthoclase in an amount of ~39%), subhedral plagioclase (~20%). In places, the phenocrysts contain minor fractures filled by quartz and partly affected by sericitization. Zircon, apatite, opaque minerals are accessories (~1%). Batkhaan rhyolites are massive and porphyritic and contain ~20% subhedral–anhedral quartz ~20% and subhedral–anhedral K-feldspar phenocrysts in a groundmass consisting of quartz, plagioclase, and K-feldspar (Fig. 3c). Delgerkhaan plutonic rocks are dominated by granite, granodiorite, and quartz monzonite. Hypidiomorphic monzogranite (sample D1742) consists of euhedral to subhedral plagioclase (~30%), subhedral K-feldspar (~30%), euhedral quartz (~20%), biotite (~13%), and hornblende (~5%), (Fig. 3d) plus accessory zircon, apatite, and titanite (~2%). Hypidiomorphic granodiorite (sample D0815) consists of plagioclase (~45%), K-feldspar (~20%), subhedral quartz (~15%), hornblende (~10%) and biotite (~8%) (Fig. 3e, f) plus accessory zircon and opaque minerals and secondary sericite and chlorite (~2%). The Zambalkhudag coarse-grained granodiorite (sample D1726) consists of subhedral plagioclase (~39%), euhedral to subhedral K-feldspar (~20%) and anhedral quartz (~20%), hornblende (~10%) and biotite (~10%) plus secondary chlorite (Fig. 3g, h). In places, plagioclase and K-feldspar form myrmekite textures. Accessory minerals are zircon and apatite (~1%). The volcanic rocks associated with the Delgerkhaan pluton are dominated by porphyry andesite and trachyandesite. Andesite (Sample D1737) contains 0.2–1 mm long subhedral phenocrysts of plagioclase (~50%) partly replaced by sericite (Fig. 3i). The groundmass (~50%) consists of K-feldspar, plagioclase laths, biotite, and secondary chlorite and hornblende (Fig. 3i).

4.1 U-Pb geochronology

The separated zircon grains are stubby to elongated and euhedral to subhedral. Their sizes range from 50 to 300 μm and the aspect ratio vary from 1.5 to 3. The grains are transparent, mostly colorless or yellowish to brownish. In CL images most grains exhibit fine to coarse banded oscillatory zoning (Fig. 4), although there are also zircons with patchy or sectorial zoning. The undifferentiated granitoids have one zircon grain with 498 Ma, and the rest of the zircons yielded U-Pb zircon concordia age of 296 ± 3 Ma (Fig. 5). The Batkhaan volcano-plutonic suite carries zircons whose U-Pb concordia ages range from 282 to 274 Ma. The concordia ages of zircons from the samples of the Delgerkhaan volcano-plutonic suite and Zambalkhudag pluton are bracketed between 220 and 224 Ma. Zircon features of each sample and their yielded ages are listed in Table 2. Zircon dating results are shown in Supplementary Table 2.

4.2 Whole-rock geochemistry

4.2.1 Undifferentiated granitoids

The major and trace element geochemical data of the studied samples are given in Supplementary Table 3. The undifferentiated granitoids of the study area are characterized by medium SiO_2 (65.7–66.7 wt%), Al_2O_3 (15.0–16.7 wt%), and low TiO_2 (0.39–0.61 wt%). The contents of MgO and FeO^T range from 0.61 to 1.29 and from 2.58 to 3.94 wt%, respectively, resulting in Fe numbers of 0.75 to 0.83 [Fe# = $FeO^T/(FeO^T + MgO)$] and Mg numbers of 44 to 56 [Mg# = molar 100 × Mg/(Mg + Fe)]. The total alkalis ($Na_2O + K_2O$) are high (7.9–8.3 wt%), in the TAS diagram they plot in the field of quartz monzonite (Fig. 6a). The rocks are ferroan to magnesian (Fig. 6c) and high-K calc-alkaline (Fig. 6d). They belong to I-type granites, and the ratio of A/CNK [molar $Al_2O_3/(CaO + K_2O + Na_2O)$] ranges from 0.94 to 1.04 indicating their metaluminous to the weakly peraluminous character (Fig. 7b). The rocks exhibit high concentrations of Sr (519–1377 µg/g) and low concentrations of Y (9.9–18.7 µg/g) and Yb (0.75–1.87 µg/g). In addition, they have low Cr (< 20 µg/g), and Ni (<20 µg/g). The degree of LREE and HREE differentiation is moderate to high with [$(La/Yb)_{CN}$ = 11–32] (Fig. 8a). The REE patterns show weak negative to zero Eu anomalies. The primitive mantle-normalized multi-element patterns show enrichment in incompatible elements and positive Nb anomalies relative to Th and La (Fig. 8b).

4.2.2 Batkhaan volcano-plutonic rocks

The Batkhaan granitoids geochemically consist of granites and monzonites (Fig. 6a). The SiO_2 content of the Batkhaan granitoids are spans 72.9–77.2 wt%, and total alkalis are 7.46–9.77 wt%. The rocks have low Al_2O_3 (11.3–14.9 wt%), Mg# (14–39), and CaO (0.08–0.78 wt%), but high Fe# (0.86–0.96 wt%), i.e., they represent ferroan rocks and normal to high-K calc-alkaline (Fig. 6c, d). Compared to the granites, the monzonites have lower SiO_2 (59.5–61.4 wt%) and total alkalis (6.86–7.72 wt%), but higher Al_2O_3 (16.6–19.7 wt%) and Mg# (26–36) and CaO (3.4–5.9 wt%). The volcanic rocks are dominantly rhyolite except for one sample of dacite (Fig. 6b). They belong to A-type granites (Fig. 7a, b) and their A/CNK values range from 0.95 to 1.13, indicating peralkaline, metaluminous, and peraluminous transition character (Fig. 7c). They have high SiO_2 = 67.9–77.6 wt%, and total alkalis = 6.5–8.8 wt%, but low Al_2O_3 (11.2–13.6 wt%), Mg# (10–39), and CaO (0.05–1.75 wt%). All Batkhaan rocks, both plutonic and volcanic, have slightly LREE enriched [$(La/Yb)_{CN}$ = 2.8–6.6, except D1721 = 23.5] with clear troughs at Eu (Fig. 8c). They are enriched in Nb (0.8–25 μg/g), Zr (71–411 μg/g), Y (3.6–56 μg/g), U (0.82–4.91 μg/g), and Ta (0.2–1.79 μg/g), but depleted in Sr (17–263 μg/g in granites and 245–456 μg/g in monzonites). The primitive mantle normalized spidergrams of the Batkhaan rocks show deep troughs at Ba, Sr, P, Eu, and Ti and shallower troughs at Nb and Ta (Fig. 8d).

4.2.4 Delgerkhaan volcano-plutonic rocks

Previous researchers considered the Delgerkhaan and Zambalkhudag plutons as different (Tumurchudur et al., 2006). In this paper, we characterize them together since they possess similar geochemical features. The rocks of the Delgerkhaan and Zambalkhudag plutons span wide ranges of SiO_2 (61.4–75 wt%) and total alkalis ($Na_2O + K_2O$ = 6.3–9.4 wt%), a restricted range of Al_2O_3 (12.9–16.60 wt%). Most of the samples are characterized by high TiO_2 (0.03–0.82 wt%), moderate FeO^T (1.0–5.3 wt%), and high Mg# (44–73) except for three samples with lower Mg# (2.85–24). In the TAS diagram, the granitoids fall in the fields of granodiorite, quartz monzonite, and granite (Fig. 6a). As Fe# ranges from 0.53 to 0.99, the granitoids belong to the magnesian type and high-K cal-alkaline series granites (Fig. 6c, d). The samples plot on the I-type granite field (Fig. 7a, b) and in the A/CNK versus the A/NK diagram, the samples plot in the metaluminous and I-type fields (Fig. 7c, d). The chondrite normalized REE patterns show fractionated LREE [$(La/Gd)_{CN}$ = 2.1–9.7], less fractionated HREE [$(Gd/Yb)_{CN}$ = 1.2–6.5], and weak to zero negative or positive Eu anomalies (Fig. 8e). The spidergrams show enrichment in LILEs and depletion in HFSEs. They display lower contents of Nb, Zr, Y, and U but higher Sr and Pb (Fig. 8f). The samples are characterized by high Sr (168–598 μg/g), and low Y (6.1–35 μg/g), and Yb (1.09–4.04 μg/g). The volcanic rocks associated with the Delgerkhaan pluton have SiO_2 = 58.5–68.1, MgO = 0.50–7.4, Al_2O_3 = 13.6–16.2, TiO_2 = 0.6–1 wt%, FeO^T = 4.16–7.4, ($Na_2O + K_2O$) = 5.18–8.6 wt. %. The values of Mg# and Fe# are bracketed between 22 and 79, 0.5 and 0.93, respectively. The volcanic rocks are andesite, trachyandesite, trachydacite, and dacite (Fig. 6b). According to A/CNK (0.77–1.07), they represent metaluminous to peraluminous varieties (Fig. 7c). The chondrite normalized REE patterns (Fig. 7a) show enrichment in LREEs [$(La/Yb)_{CN}$ = 2.88–34.6], and weak negative to positive Eu anomalies. The multi-element patterns show negative Nb and Ti anomalies (Fig. 8e) and significant enrichment in LILE (K, Rb, Ba, Sr) (Fig. 8f).

4.3 Zircon Hf isotopes

Seven analyses from sample D0925 gave initial $^{176}Hf/^{177}Hf$ ratios (t = 296 Ma) varying from 0.282488 to 0.282654, among which one analysis on an inherited zircon grain with an age of ~498 Ma yielded initial $^{176}Hf/^{177}Hf$ ratios (t = 498 Ma) of 0.282488 (Supplementary Table 4). Their εHf(t) values and two-stage model (T_{DM2}) ages range from −2.26 to + 2.6 and from 1168 to 1527

Ma, respectively. The initial $^{176}Hf/^{177}Hf$ ratios for 15 spots of the ~280 Ma Batkhaan granitoids and associated rhyolites (samples D1710 and D1709, respectively) vary from 0.282664 to 0.282918. The corresponding εHf(t) values and two-stage model ages T_{DM2} vary from 2.14 to 11.22 and 581 to 1159, respectively. Twenty-one analyses of three samples from the 220–240 Ma Delgerkhaan granites (samples D1718, D1726, and D1742) yielded initial $^{176}Hf/^{177}Hf$ ratios from 0.282684 to 0.282830, which are translated into εHf(t) values from + 1.9 to + 7.09 and T_{DM2} between 810 and 1139 Ma, respectively.

4.4. Sm-Nd isotopic analysis

The Sm-Nd isotopic analysis was carried out for 5 selected samples. One sample from each granitic massif, and one from the Batkhaan rhyolite. The $\varepsilon_{Nd}(t)$ values are calculated using the zircon U-Pb concordant ages of each sample. The sample from undifferentiated granitoids has $\varepsilon_{Nd}(t)$ = −1.7 and corresponds to $T_{Nd(DM)}$ = 1076 and $T_{Nd(C)}$ ages of 1262 Ma (Supplementary Table 4). The Batkhaan granite and rhyolite have higher $\varepsilon_{Nd}(t)$ values varying from + 2.7 to + 4.1. They have $T_{Nd(DM)}$ model ages of 762–993 Ma and $T_{Nd(C)}$ model ages of 725–838 Ma. The remained samples exhibit $\varepsilon_{Nd}(t)$ values ranging from −0.7 to + 1.7 corresponding to $T_{Nd(DM)}$ model ages of 697–1509 Ma and $T_{Nd(C)}$ model ages of 893–1073 Ma.

5. Discussion

5.1 Three groups of granitoid magmatism

Our new U-Pb age results allow us to recognize three groups of magmatism in the Delgerkhaan area from the Early Permian until the Late Triassic: at ~296, ~280, and ~230 Ma. The Group I formed at 296 ± 3 Ma intrusion was previously considered as Late Cambrian (Dagvadorj et al., 1993), but our new data show that it has Early Permian age. Moreover, the granitoids contain Late Cambrian (Furongian) inherited zircons (~498 Ma), implying that melt is including zircons that crystallized in the past. Group II includes the Batkhaan granite, monzonites, and associated rhyolites of 282 ± 3 and 274 ± 2 Ma, respectively (Fig. 5). These ages are generally consistent with the age of 282 ± 16 Ma, previously reported for the granodiorite although with a large error (Amar-Amgalan, 2008). Group III comprises the Delgerkhaan pluton of 230–240 Ma. The Zambalkhudag pluton was previously speculated as Late Carboniferous, as it intrudes Devonian sandstones containing fauna (Tumurchudur et al., 2006 and reference therein), however, our data show that it formed at 220 ± 2 Ma. Thus, we suggest that the Zambalkhudag pluton is coeval and related to the Delgerkhaan pluton as they possess similar geochemical and isotopic features and close crystallization ages (Table 2; Figs. 5, 6). This group of magmatism also includes associated ~223 Ma (K-Ar) of intermediate volcanics (Dagvadorj et al., 1993).

5.2 Petrogenesis and sources

5.2.1 Group I (~296 Ma granitoids)

Group I granitoids are metaluminous to peraluminous and have an I-type trend in the Th versus Rb diagram (Figs. 6, 7c). Two samples have elevated Rb, K, U, and Th concentrations and low MgO, Cr, and Ni contents implying crustal compositional affinities. In addition, the values of Nb/Ta (9.4–11) and Zr/Hf (38–39) differ from those of the primitive mantle (Nb/Ta = 17.8; Zr/Hf = 45), and closer to the crustal values (Nb/Ta = 11; Zr/Hf = 33), thereby supporting a crustal source for their parental magma. Their chondrite-normalized REE patterns are enriched in the LREEs, depleted in the HREEs, and show no Eu and Sr anomalies (Fig. 8a) precluding fractionation of plagioclase. The primitive-mantle normalized multi-element patterns show pronounced negative anomalies at Nb, Ta, and Ti (Fig. 8b), which are typical of supra-subduction igneous rocks. Nevertheless, one sample has low K_2O, U, Th, and their Nb/Ta (16) and Zr/Hf (45) ratios are closer to those of the primitive mantle. Although the number of samples is not enough to discuss their petrogenesis in detail, we suggest that the undifferentiated body of Group I may consist of granitic bodies derived from two types of sources: felsic (recycled) and mafic (mixed or juvenile). The two granitoids of Group I have mostly negative values of $\varepsilon_{Nd}(t)$ (−1.7) and $\varepsilon_{Hf}(t)$ (−3.57 to +2.3), and Neoproterozoic to Mesoproterozoic modal ages implying the presence of ancient crust material in their source (Fig. 9a, b).

5.2.2 Group II (Batkhaan)

In Group II, we consider the Early Permian Batkhaan granitoids, monzonites, and rhyolites together as they have close ages and similar geochemical features (Figs. 6, 7; Supplementary Table 3) and therefore they probably formed in similar tectonic settings. The Group II rock association is characterized by high total alkalis, Fe#, Ga/Al, HFSE (Zr, Nb, and Y) and REEs low CaO, Ba, and Sr, and clear negative Eu anomaly (Fig. 8c, d). These features suggest that they have characteristics similar to A-type granites (Fig. 7a, b). The origin, evolution, and tectonic settings of formation/emplacement of A-type granites remain debatable though (e.g., Bonin, 2007). They can be produced by: (1) fractionation of mantle-derived magmas with or without interaction with crustal rocks (Turner et al., 1992); (2) low degrees of partial melting of lower crustal or underplated basaltic magma (Jones et al., 2018); (3) hybrid magma from the mantle and crustal derived melts and metasomatism of granitic magmas (Taylor and McLennan, 1995).

The Group II rocks show no coeval mafic igneous rocks, as should be expected for extensive fractional crystallization. Restricted variations of zircon $\varepsilon Hf(t)$ values exclude the mixing of mantle-derived and crust-derived melts as that would have generate melts with scattered isotopic signatures (e.g., Kemp et al., 2007). The low Nb, Ta, and Ti and high Th, U, and Pb contents, high trace element ratios of Th/Ce (0.18–0.31) and Th/La (0.4–0.86) ratios suggesting a significant contribution of the continental crust during their generation. The monzonites of Group II show different geochemical characteristics, such as the lack of Eu anomaly, the low contents of K_2O, Th and Rb, and Th/Ce (0.11–0.14) and (Th/La) (0.24–0.29) ratios lower than those in granites and rhyolites and closer to those of basaltic rocks (Rudnick and Gao, 2003). We suggest that the Group II monzonites formed through the partial melting of a mafic source.

Experimental data indicate that metaluminous and peraluminous A-type magmas like Group II granites and rhyolite samples can be produced by the melting of calc-alkaline tonalite and granodiorite at shallow depths (4 kbar) and high temperatures (950 °C) (Patiño Douce, 1997). In fact, the low $(La/Yb)_{CN}$ ratios as well as the pronounced negative anomalies of Ba, Eu, and Sr (Fig. 8c, d) of Group II rhyolites and granites with metaluminous to peraluminous compositions indicate that they formed at shallow crustal depths (Bonin, 2007). Group II rocks exhibit the positive value of $\varepsilon_{Hf}(t)$ (+2.14 to +9.76) and $\varepsilon_{Nd}(t)$ (+2.7 to +4.1) (Fig. 8b) and corresponding two-stage model ages suggesting that the primary magma crystallized from a Neoproterozoic juvenile source. The high temperatures of melting required to produce A-type rocks were probably provided by the underplating of juvenile mafic magmas, which fed the melting of the monzonites in the lower crust and granites and rhyolites at a shallow crustal depth.

5.2.3 Group III (Delgerkhaan)

Delgerkhaan granitoids and the Triassic volcanics show similar ages and geochemical features. The Group III calc-alkaline samples have high-K, Rb, U, and Th (Figs. 6d; 8e, f). However, compared to Group I, the Group III samples have higher Mg, Cr, and Ni, suggesting a deeper and/or more mafic source of melting. The absence of contemporaneous mafic microgranular enclaves excludes extremal fractional crystallization of mantle-derived magma. Their high Sr/Y ratio and fractionated REE pattern suggest the presence of minerals with high partition coefficients for HREE, i.e., garnet or hornblende, in the residue. The melts that equilibrate with residual garnet would have steep HREE distribution patterns and a high ratio of Yb/Lu (>10; Moyen, 2009). However, the Group III rocks show moderately steep REE distribution patterns (Fig. 8e, f) and relatively low Yb/Lu (5–7) ratios excluding the presence of garnet in the residue. The Group III REE patterns are moderately concave-upward between the MREEs and HREEs as typical of hornblende-bearing sources as hornblende is relatively MREE-rich (Macpherson et al., 2006), as can be seen on. The lower Nb/Ta and SiO_2 (Fig. 10a) can be explained by the fractionation of hornblende (Tiepolo and Vannucci, 2014). More evidence for the fractionation of hornblende comes from the Dy versus Er diagram (Fig. 10b).

The values of Fe# in the Group III rocks are relatively low (average = 0.68) compared to other groups (Fig. 6c; Frost et al., 2001). Such low Fe# granitoids are common in the Cordilleran batholiths (< 0.6) and even in the Caledonian post-orogenic granites (~0.5). As Fe# is strongly affected by differentiation during magma ascent (Frost et al., 2001), and early crystallization of Fe-bearing mineral phases would inhibit iron enrichments during differentiation. In case of Group III granitoids, we suggest that fractional crystallization of hornblende provided the formation of peraluminous I-type granitoids with lower Fe# (Chappell et al., 2012).

Diagrams La/Yb versus La and Zr/Nb versus Zr can be used to evaluate the effect and degree of fractional crystallization and partial melting on compositional variations in magmas. The sample points form trends parallel to the array of partial melting (Fig. 11a, b) suggesting that partial melting played a greater role than fractional crystallization. The Nb/Zr versus Th/Zr (Fig. 11c) and Nb/Y versus Rb/Y (Fig. 11d) systematics also confirm the participation of subducted slab-derived fluids during the magma generation.

The combination of these features with the enrichment of Group III rocks in LREEs and LILEs and depletions in HREEs and HFSEs (Fig. 8e, f) suggests that these rocks resulted from the partial melting of lower crustal source with hornblende in residue and participation of subduction-related fluids. As the Group III samples are characterized by positive $\varepsilon_{Hf}(t)$ and positive to negative $\varepsilon_{Nd}(t)$ (Fig. 9a, b), and Neoproterozoic two-stage model ages, we conclude that their primary magma originated by the partial melting of Neoproterozoic depleted lower crust.

5.3 Nd-Hf isotope decoupling

Hf and Nd crustal modal ages of studied three group samples exhibit that pre-existing juvenile material contribution was Mesoproterozoic and mainly Neoproterozoic (Fig. 12a). The values of εHf(t) for zircons from the rocks of the Group II and III deviate positively from the whole-rock $\varepsilon_{Nd}(t)$ values compared to the normal terrestrial arrays for the mantle and crust Nd-Hf isotope evolution (Fig. 12b; Vervoort et al., 1999) suggesting Nd-Hf isotope decoupling (e.g., Schmitz et al., 2004). There are three main explanations for the decoupled Nd-Hf isotopic compositions in the granitoids under consideration. The first implies the presence of garnet capable to decouple Nd and Hf isotopes in the source (Schmitz et al., 2004). As Lu in garnet has a higher coefficient of distribution compared to Sm, Nd, and Hf, residual garnet can retain Lu over time and produce high $^{176}Hf/^{177}Hf$ melt reservoirs. The magmas derived from such garnet-bearing residual assemblages may have higher $^{176}Hf/^{177}Hf$ relative to $^{143}Nd/^{144}Nd$. No evidence for residual garnet was exhibited in the Group II and III rock associations and it rules out this model.

Another hypothesis explains such decoupling by the melting of a meta-sedimentary source with a high Lu/Hf ratio because of the "zircon effect". As zircon is resistant to weathering it can preserve its primary magmatic Hf isotopic composition (Rubatto and Hermann, 2003). The retention of radiogenic Hf in igneous zircons is possible during the partial melting of juvenile crustal material (Patchett and Tatsumoto, 1981). Zircons retain Hf isotope signatures, acquired during their crystallization from an earlier magma, whereas the whole-rock Sm-Nd system is typically equilibrated with later melts and hence produces lower $\varepsilon_{Nd}(t)$ values (Wu et al., 2006). As a result, the granites have less radiogenic whole-rock Nd isotope compositions than the normal terrestrial rocks at a given value of $\varepsilon_{Hf}(t)$ in zircon. Such a scenario for the decoupling of zircon Hf and whole-rock Nd isotopes can be attributed to the Group II granitoids. These granitoids have high Lu/Hf ratios of 0.07 to 0.11, i.e. similar to those of meta-sedimentary rocks, 0.09 to 0.11 (Eroğlu et al., 2013), suggesting the participation of sediments. The crustal extension could involve sediments into magma generation, and change the proportion of Hf and Nd isotopes in the melt. However, this scenario cannot be responsible for Group III rock association as they have lower Lu/Hf ratios (0.02–0.07) than meta-sedimentary sources.

An alternative hypothesis is the partial melting of decoupled Nd-Hf-bearing lithospheric mantle or juvenile lower crust. This hypothesis defends that decoupled compositions are inherited from the interaction between fluids (with high Nd/Hf ratios from subducting sediments or oceanic crust) and the lithospheric mantle (Chauvel et al., 2009) as Hf is less mobile in slab-derived fluid than Nd resulting in the re-enrichment of Nd isotopes. Consequently, fluids extracted from subducted sediments or slabs and affecting the mantle wedge would generate melts with high $\varepsilon_{Hf}(t)$ and low $\varepsilon_{Nd}(t)$ (Chauvel et al., 2009). We consider such a fluid-mantle interaction as a reason for the Nd-Hf decoupled composition of the Group III rocks.

5.4 Tectonic model

The geochemical and isotope compositions of the three groups of igneous rocks of the Khangay–Khentey basin in the Central Mongolia suggest different tectonic settings of their emplacement. The tectonic setting of the formation of Group I rocks remains enigmatic as we have data from three samples only. In the tectonic discrimination Nb versus Y and Rb versus Y + Nb diagrams, most samples of Group II plot in the field of post-collisional granites (Fig. 13a). However, the post-collisional setting is an unlikely hypothesis since, so far, no evidence of collision has been found in the adjacent areas, e.g., significant crustal thickening, abundant S-type granites, etc. Moreover, the amount of outcropped A-type granites and rhyolites in the study area is relatively small, although post-collisional settings are characterized by compositionally variable and huge volume of granitoids. The Group II samples show high Ce/Nb, Y/Nb, and Ga/Nb ratios and therefore represent A_2-type granitoids (Fig. 14a, b). Felsic igneous rocks formed at convergent margin settings may also exhibit A-type signatures. For example, the A-type granites of the Lachlan Belt in eastern Australia were emplaced in a back-arc extensional setting in response to slab roll-back (e.g., Collins et al., 2020). Although the petrogenesis of Group II (A_2-type) may support such a scenario, we think the magmatism found is not sufficiently important. Usually, a back-arc extension setting is precluded by a vast subduction-related granitoid batholiths emplacement, like those of the Eastern Sikhote-Alin or the Andes. The Group I granitoids are older than the Group II ones, but the outcrops of the former are small and pre-Early Permian granitic bodies are scarce in Central Mongolia as well (Fig. 1c). Therefore, we assume that the Group II rocks emplaced in a setting of local extension possibly linked with magma underplating and /or asthenospheric upwelling.

The Group III high-potassium calc-alkaline I-type granitoids with low Fe# could be emplaced in two tectonic settings: (1) Andean-type active continental margin, (2) post-collisional (Frost et al., 2001). The Group III granites are compositionally close to andesite and trachyandesite (Fig. 2), and enriched in LREEs and LILEs, but depleted in HFSEs (e.g., Nb, Ta, and Ti) (Fig. 7, 8). In the Nb versus Y (Fig. 13a) and Th/Yb versus Ta/Yb (Fig. 13b) diagrams, they plot in the volcanic arc granite field and active continental margin field, respectively. These characteristics suggest their emplacement in a subduction-related tectonic setting, although post-collisional granites also show arc-like trace element signatures due to the contribution of subduction-related materials from previous tectonic events. However, recent studies have shown that the Mongol–Okhotsk Ocean remained open until the Middle Triassic. The evidence for this comes from: (1) Middle Triassic subduction-related magmatism manifested on its both sides, northern (e.g., Donskaya et al., 2013) and southern (e.g., Zhu et al., 2016; Liu et al., 2018); (2) zircon ages from metasediments (turbiditic and greywacke sandstones) in the eastern part of the Mongol–Okhotsk belt, which peak at ~173 Ma, indicating that sedimentation of the Mongol–Okhotsk oceanic basin continued until the Middle Jurassic (e.g., Sorokin et al., 2020); (3) paleomagnetic data from the volcanic rocks of NE Mongolia reveal that the Central Mongolia Block was separated from the Siberian Craton by the MOO with a ~30° latitudinal difference in the Early Permian and welded in the Middle Jurassic (e.g., Yi and Meert, 2020); (4) coexistence of Boreal-type realm (northern cold affinity) and Tethyan-type realm (southern warm affinity) Anisian (Middle Triassic) ammonoid fauna in the Khentey province suggests that a wide ocean still existed during the Middle Triassic (Ehiro et al., 2006). The study area lies about 150 km to the west from Adaatsag ophiolite–a suture of the Mongol–Okhotsk Ocean. Besides, the study area is adjacent to the Central Mongolia–Erguna Block from the south (e.g., Wilhem et al., 2012). Therefore, present-day data do not support a post-collisional origin for Group III rocks. Consequently, we think that an Andean-type active continental margin explains better the characteristics of Group III.

5.5 Geodynamic implications

The three groups of magmatic felsic rocks that crop out in the Khangay–Khentey basin of Central Mongolia formed during the Late Paleozoic to the Early Mesozoic in different tectonic settings. The Late Carboniferous to Early Permian A-type granites and highly alkaline igneous rocks are widely distributed south of the Main Mongolian Lineament (South Mongolia and Inner Mongolia) and have been considered as a part of the Tarim Large Igneous Province (LIP) (Yarmolyuk et al., 2014). However, unlike the Tarim LIP, the Khangay–Khentey lacks alkaline basalt, comendite, pantellerite, or nepheline syenite and A_1-type granitoids, which are considered as a result of a mantle plume. Thus, the Batkhaan igneous rocks were emplaced in a setting of weak local extension rather than in relation to a plume-induced rifting. The pre-Permian geological structures of the central CAOB were related to the evolution of the PAO and the subsequent suturing of the MOO (Windley et al., 2007). The Late Paleozoic to Early Mesozoic subduction of the MOO crust formed the magmatic fields outcropped in the Khangay–Khentey region (Fig. 1c) (e.g., Donskaya et al., 2013; Zhao et al., 2017). The northward subduction of the MOO lithosphere beneath the Siberian Craton (including its accreted southern margin) has been well-defined, as indicated by the subduction-related Angara-Vitim granitoids and the Permian–Triassic Selenge volcano-plutonic belt (e.g., Donskaya et al., 2013; Izbrodin et al., 2020). These magmatic belts were emplaced by several episodes during a period from the Late Carboniferous to the Jurassic. Unlike the northern part of Mongolia–Okhotsk suture zone, the tectonic evolution of the southern part has been better reconstructed in the Erguna Belt, NE China (Sun et al., 2013; Liu et al., 2018), and to a lesser extent, in the Khangay Belt (e.g., Dolzodmaa et al., 2020). According to the igneous rock ages, the southern subduction of the Mongol–Okhotsk oceanic crust started in the Carboniferous and continued until the Early–Middle Jurassic (Liu et al., 2018).

U-Pb ages, geochemical, and isotope data from Group III granitoids agree with the previous data and indicate a magmatic emplacement in the Early Permian–Late Triassic time. In addition, there is no systematic WE younging of magmatic ages in the southern segment of the Mongol–Okhotsk Belt (Fig. 1c). Consequently, the Group III rocks probably formed during the southward subduction of the MOO lithosphere in a tectonic setting of an Andean-type active continental margin. Our new data support the idea of the subduction of the Mongol–Okhotsk oceanic crust beneath the Central Mongolia–Erguna Block during the Early Permian–Late Triassic from the Mongolian side.

6. Conclusions

Our new U-Pb zircon ages, whole-rock geochemical data, and in situ Hf-in-zircon and whole-rock Sm-Nd isotope characteristics obtained from Late Paleozoic–Early Mesozoic granitoids of Khangay–Khentey basin in Central Mongolia allowed us to conclude the following.

(1) Late Paleozoic-Early Mesozoic granitic rocks in the Khangay–Khentey basin formed at three different times, which were emplaced in Early Permian (~296 Ma, Group I), middle Permian (~280 Ma, Group II), and middle Triassic (~230 Ma, Group III), respectively.

(2) Group I includes I-type quartz monzonite and granodiorites derived from crustal (recycled) and mantle (mixed or juvenile) sources and their Cambrian age is superseded.

(3) Group II pluton comprises A_2-type granites, monzonites, and rhyolites. Monzonites were derived from a mafic source, whereas granites and rhyolites were derived from a source containing Neoproterozoic crustal materials and depleted mantle material. The Group II granitoids were emplaced in a local extension environment linked with magmatic underplating and/or asthenosphere upwelling.

(4) Group III includes I-type granitoids and volcanic rocks. They were generated from partial melting of a juvenile lower crustal source with the contribution of ancient crust. They formed at an Andean-type active continental margin related to the southward subduction of the Mongol–Okhotsk Ocean beneath the Central Mongolia–Erguna Block.

Acknowledgment

This research was supported by CNEAS and FRIS of Tohoku University and in part by grants from the MEXT/JSPS KAKENHI JP18H01299 and JP21H01174 to TT and JP19K04043 to KA, by the National Natural Science Foundation of China (grant number 41772230) to L. Miao, and by the Russian Science Foundation (grants 20-77-10051 to Ilya S. and 21-77-20022 to Inna S.). AG gratefully acknowledges the Japanese Government MEXT Scholarship. We also thank Isamu Morita, and Manzshir Bayarbold, Sanchir Dorjgochoo for their assistance in the laboratory and for providing geological material. Contribution to IGCP#662.

CAPTIONS

Fig. 1. (a) Tectonic outline of Asia and location of the Central Asian Orogenic Belt (modified from Safonova, 2017). (b) Location of large granitic batholiths in the eastern segment of the CAOB (modified from Yarmolyuk et al., 2002). (c) Late Paleozoic–Early Mesozoic granitoid distribution in Central and Northeastern Mongolia. Published zircon ages are also shown; the references are summarized in Supplementary Table 1. MOB–Mongol–Okhotsk Belt.

Fig. 2. Simplified geological map of the Delgerkhaan area (modified after the 1:200 000 State Geological Map), showing sample locations.

Fig. 3. Photomicrographs of cross-polarized light view showing textures and mineral assemblage of the studied samples from the Khangay–Khentey basin. (a) Granodiorite (sample D0925); (b) Syenogranite (sample D1710); (c) Rhyolite (sample D1709); (d) Monzogranite (sample D1742); (e) Granodiorite (sample D0815); (f) Granodiorite (sample D0817); (g) Monzogranite (sample D1718); (h) Granodiorite (sample D1726); (f) Andesite (sample D1745). Bt—biotite; Hbl—hornblende; Kfs—K-feldspar; Pl—plagioclase; Qz—quartz; Ms—muscovite.

Fig. 4. Cathodoluminescence (CL) images of representative zircon crystals from the studied samples from the Khangay–Khentey basin. White circles show individual analysis spots, corresponding Pb–Pb ages and yellow circles show an individual spot of Lu-Hf isotope and their $\varepsilon_{Hf}(t)$ values.

Fig. 5. Concordia diagrams of zircons for samples from the Khangay–Khentey basin, showing U-Pb isotope ratios. Light grayish ellipses indicates discordant data excluded from the calculation.

Fig. 6. Major element discrimination diagrams showing the compositions and characteristics of the studied samples from Khangay–Khentey basin, Central Mongolia. (a) SiO_2 versus (Na_2O + K_2O) total alkali-silica (TAS) diagram for plutonic rocks (after Irvine and Baragar, 1971), (b) SiO_2 versus (Na_2O + K_2O) total alkali-silica (TAS) diagram for volcanic rocks (after Le Bas et al., 1986), (c) $FeO^T/(MgO + FeO^T)$ wt% versus SiO_2 plot (after Frost et al., 2001), (d) K_2O wt% versus SiO_2 wt% plot (Peccerillo and Taylor, 1976).

Fig. 7. (a) (Na_2O + K_2O)/CaO versus $10^4 \times$ Ga/Al and (b) Zr versus $10^4 \times$ Ga/Al (after Whalen et al., 1987)
discriminating A-type granites from I, S type granites; (c) A/CNK [molar $Al_2O_3/(CaO \times Na_2O \times K_2O)$] versus A/NK [molar $Al_2O_3/(Na_2O \times K_2O)$] diagram, the boundary line is from Maniar and Piccoli (1989); (d) Rb versus Th diagrams for the studied samples from the Khangay–Khentey basin.

Fig. 8. CI-chondrite-normalized REE patterns and primitive-mantle-normalized trace element spidergrams for the studied samples from the Khangay–Khentey basin. Both chondrite and primitive-mantle normalized values are from Sun and McDonough (1989).

Fig. 9. (a) Correlations between whole-rock $\varepsilon_{Nd}(t)$ and concordia ages. (b) Correlations between $\varepsilon_{Hf}(t)$ and Pb–Pb ages of zircons for the studied samples from the Khangay–Khentey basin.

Fig. 10. (a) Nb/Ta versus SiO_2 and (b) Er versus Dy diagrams showing hornblende fractionation for the Group III rock association from the Khangay–Khentey basin.

Fig. 11. (a) Plots of La/Yb versus La; (b) Zr/Nb versus Zr; (c) Nb/Zr v versus Th/Zr; (d) Rb/Y versus Nb/Y for the Group I and III rock associations from the Khangay–Khentey basin.

Fig. 12. (a) Histogram shows zircon U-Pb age, two-stage crustal Hf, and Nd model ages; (b) Plots of whole-rock $\varepsilon_{Nd}(t)$ versus zircon $\varepsilon_{Hf}(t)$ of the studied samples from the Khangay–Khentey basin. The terrestrial array is from Vervoort et al. (1999).

Fig.13. Tectonic discrimination diagrams for the studied samples from the Khangay–Khentey basin in Central Mongolia: (a) Nb versus Y (Pearce et al., 1984); (b) Th/Yb versus Ta/Yb (Pearce et al., 2008). Syn-COLG–syn-collision granite; VAG–volcanic arc granite, WPG–within plate granite, Post-COLG–post-collisional granite; ACM–active continental margin; DM–depleted mantle; EM–Enriched mantle.

Fig. 14. (a) Ce/Nb versus Y/Nb and (b) 3 × Ga–Nb–Y subdivision diagrams (after Eby, 1992) for A-type granites for the Group II rock association from the Khangay–Khentey basin. A_1–continental rift or intra-plate magmatism related granite; A_2– post-collisional setting or island-arc related granite. IAB–island arc basalt; OIB–oceanic island basalt.

Table 1. Mineral assemblage and contents of studied samples of the Khangay–Khentey basin.

Table 2. Summary of zircon characteristics of dated samples and corresponding ages.

Supplementary Table 1. Radiometric ages in the literature of the Late Paleozoic–Early Mesozoic granitoids in Central and Northeast Mongolia.

Supplementary Table 2.

LA-ICPMS U–Th–Pb analytical data for zircons of the studied samples from the Khangay–Khentey basin. * Discordant data excluded from calculation.

Supplementary Table 3.
Major (wt%) and trace (µg/g) element compositions including sample location and rock type of the studied samples from the Khangay–Khentey basin.

Supplementary Table 4. Zircon Lu-Hf and whole-rock Sm-Nd isotope data of the studied samples from the Khangay–Khentey basin.

REFERENCES

Amar-Amgalan, S., 2008. U-Pb geochronology and multi-isotopic systematics of granitoids from Mongolia, Central Asian Orogenic Belt: Implications for granitoid origin and crustal growth during the Phanerozoic. Unpublished Ph.D. thesis. Okayama University, Japan, p.162.

Aoki, S., Aoki, K., Tsujimori, T., Sakata, S., Tsuchiya, Y., 2020. Oceanic-arc subduction, stagnation, and exhumation: zircon U-Pb geochronology and trace-element geochemistry of the Sanbagawa eclogites in central Shikoku, SW Japan. Lithos, 358, 105378. https://doi.org/10.1016/j.lithos.2020.105378

Badarch, G., Cunningham, W.D., Windley, B.F., 2002. A new terrane subdivision for Mongolia: implications for the Phanerozoic crustal growth of Central Asia. Journal of Asian Earth Sciences, 21, 87-110. https://doi.org/10.1016/S1367-9120(02)00017-2

Black, L.P., Kamo, S.L., Allen, C.M., Aleinikoff, J.N., Davis, D.W., Korsch, R.J., Foudoulis, C., 2003. TEMORA 1: a new zircon standard for Phanerozoic U-Pb geochronology. Chemical geology, 200, 155-170. https://doi.org/10.1016/S0009-2541(03)00165-7

Bonin, B., 2007. A-type granites and related rocks: evolution of a concept, problems and prospects. Lithos, 97, 1-29. https://doi.org/10.1016/j.lithos.2006.12.007

Bouvier, A., Vervoort, J.D., Patchett, P.J., 2008. The Lu-Hf and Sm-Nd isotopic composition of CHUR: constraints from unequilibrated chondrites and implications for the bulk composition of terrestrial planets. Earth and Planetary Science Letters, 273, 48-57.

Bussien, D., Gombojav, N., Winkler, W., Von Quadt, A., 2011. The Mongol–Okhotsk Belt in Mongolia—an appraisal of the geodynamic development by the study of sandstone provenance and detrital zircons. Tectonophysics, 510, 132-150. https://doi.org/10.1016/j.tecto.2011.06.024

Chappell, B.W., Bryant, C.J., Wyborn, D., 2012. Peraluminous I-type granites. Lithos, 153, 142-153. https://doi.org/10.1016/j.lithos.2012.07.008

Chauvel, C., Marini, J.C., Plank, T., Ludden, J.N., 2009. Hf-Nd input flux in the Izu-Mariana subduction zone and recycling of subducted material in the mantle. Geochemistry, Geophysics, Geosystems, 10. https://doi.org/10.1029/2008GC002101

Chen, G.N., Grapes, R., 2007. Granite genesis: in-situ melting and crustal evolution, first ed. Springer. Dordrecht, Netherlands.

Clemens, J.D., Stevens, G. and Bryan, S.E., 2020. Conditions during the formation of granitic magmas by crustal melting–hot or cold; drenched, damp or dry?. Earth-Science Reviews, 200, 102982.

Collins, W.J., Huang, H.Q., Bowden, P., Kemp, A.I.S., 2020. Repeated S–I–A-type granite trilogy in the Lachlan Orogen and geochemical contrasts with A-type granites in Nigeria: implications for petrogenesis and tectonic discrimination. Geological society, london, special publications, 491, 53-76. https://doi.org/10.1144/SP491-2018-159

Dagvadorj, D., Bold, G., Chuluun, D., Gundsambuu, Ts., 1993. Geological Map of the Central and Eastern Mongolia, Scale 1:500,000. Institute of Geological Research Regional Geological Sector, Ministry of Heavy industrial (in Mongolian).

Dagva-Ochir, L., Oyunchimeg, T.U., Enkhdalai, B., Safonova, I., Li, H., Otgonbaatar, D., Tamehe, L.S., Sharav, D., 2020. Middle Paleozoic intermediate-mafic rocks of the Tsoroidog Uul'accretionary complex, Central Mongolia: Petrogenesis and tectonic implications. Lithos, 376, 105795. https://doi.org/10.1016/j.lithos.2020.105795

Dolzodmaa, B., Osanai, Y., Nakano, N., Adachi, T., 2020. Zircon U-Pb geochronology and geochemistry of granitic rocks in central Mongolia. Mongolian Geoscientist, 50, 23-44. https://doi.org/10.5564/mgs.v50i0.1327

Donskaya, T.V., Gladkochub, D.P., Mazukabzov, A.M., Ivanov, A.V., 2013. Late Paleozoic–Mesozoic subduction-related magmatism at the southern margin of the Siberian continent and the 150 million-year history of the Mongol-Okhotsk Ocean. Journal of Asian Earth Sciences, 62, 79-97. https://doi.org/10.1016/j.jseaes.2012.07.023

Eby, G.N., 1992. Chemical subdivision of the A-type granitoids: petrogenetic and tectonic implications. Geology, 20, 641-644.

Ehiro, M., D Zakharov, Y.U., Minjni, C., 2006. Early Triassic (Olenekian) ammonoids from Khentey Province, Mongolia, and their paleobiogeographic significance. Bulletin of the Tohoku University Museum, 83-97.

Eroğlu, H., Kabadayi, Ö., 2013. Natural radioactivity levels in lake sediment samples. Radiation protection dosimetry, 156, 331-335.

Frost, B.R., Barnes, C.G., Collins, W.J., Arculus, R.J., Ellis, D.J., Frost, C.D., 2001. A geochemical classification for granitic rocks. Journal of Petrology, 42, 2033-2048.

Goldstein, S.J., Jacobsen, S.B., 1988. Nd and Sr isotopic systematics of river water suspended material: implications for crustal evolution. Earth and Planetary Science Letters, 87, 249-265.

Irvine, T.N., Baragar, W.R.A., 1971. A guide to the chemical classification of the common volcanic rocks. Canadian Journal of Earth Sciences, 8, 523-548.

Izbrodin, I., Doroshkevich, A., Rampilov, M., Elbaev, A., Ripp, G., 2020. Late Paleozoic alkaline magmatism in Western Transbaikalia, Russia: Implications for magma sources and tectonic settings. Geoscience Frontiers, 11, 1289-1303. https://doi.org/10.1016/j.gsf.2019.12.009

Jacobsen, S.B., Wasserburg, G.J., 1984. Sm-Nd isotopic evolution of chondrites and achondrites, II. Earth and Planetary Science Letters, 67, 137-150. https://doi.org/10.1016/0012-821X(84)90109-2

Jahn, B.M., 2004. The Central Asian Orogenic Belt and growth of the continental crust in the Phanerozoic. Geological Society, London, Special Publications, 226, 73-100.

Jian, P., Kröner, A., Windley, B.F., Shi, Y., Zhang, W., Zhang, L. and Yang, W., 2012. Carboniferous and Cretaceous mafic–ultramafic massifs in Inner Mongolia (China): a SHRIMP zircon and geochemical study of the previously presumed integral "Hegenshan ophiolite". Lithos, 142, 48-66. https://doi.org/10.1016/j.lithos.2012.03.007

Jochum, K.P., Weis, U., Stoll, B., Kuzmin, D., Yang, Q., Raczek, I., Jacob, D.E., Stracke, A., Birbaum, K., Frick, D.A., Günther, D., 2011. Determination of reference values for NIST SRM 610–617 glasses following ISO guidelines. Geostandards and Geoanalytical Research, 35, 397-429. https://doi.org/10.1111/j.1751-908X.2011.00120.x

Jones, M.R., Soule, S.A., Gonnermann, H.M., Le Roux, V., Clague, D.A., 2018. Magma ascent and lava flow emplacement rates during the 2011 Axial Seamount eruption based on CO_2 degassing. Earth and Planetary Science Letters, 494, 32-41. https://doi.org/10.1016/j.epsl.2018.04.044

Kemp, A.I.S., Hawkesworth, C.J., Paterson, B.A., Kinny, P.D., 2006. Episodic growth of the Gondwana supercontinent from hafnium and oxygen isotopes in zircon. Nature, 439, 580-583.

Kemp, A.I.S., Hawkesworth, C.J., Foster, G.L., Paterson, B.A., Woodhead, J.D., Hergt, J.M., Gray, C.M., Whitehouse, M.J., 2007. Magmatic and crustal differentiation history of granitic rocks from Hf-O isotopes in zircon. Science, 315, 980-983.

Kröner, A., Kovach, V., Belousova, E., Hegner, E., Armstrong, R., Dolgopolova, A., Seltmann, R., Alexeiev, D.V., Hoffmann, J.E., Wong, J., Sun, M., 2014. Reassessment of continental growth during the accretionary history of the Central Asian Orogenic Belt. Gondwana Research, 25, 103-125. https://doi.org/10.1016/j.gr.2012.12.023

Le Bas, M., Maitre, R.L., Streckeisen, A., Zanettin, B., 1986. A chemical classification of volcanic rocks based on the total alkali-silica diagram. Journal of Petrology, 27, 745-750.

Liu, H., Li, Y., He, H., Huangfu, P., Liu, Y., 2018. Two-phase southward subduction of the Mongol-Okhotsk oceanic plate constrained by Permian-Jurassic granitoids in the Erguna and Xing'an massifs (NE China). Lithos, 304, 347-361. https://doi.org/10.1016/j.lithos.2018.01.016

Macpherson, C.G., Dreher, S.T., Thirlwall, M.F., 2006. Adakites without slab melting: high pressure differentiation of island arc magma, Mindanao, the Philippines. Earth and Planetary Science Letters, 243, 581-593. https://doi.org/10.1016/j.epsl.2005.12.034

Maniar, P.D., Piccoli, P.M., 1989. Tectonic discrimination of granitoids. Geological society of America Bulletin, 101, 635-643.

Morozumi, H., 2003. Geochemical characteristics of granitoids of the Erdenet porphyry copper deposit, Mongolia. Resource Geology, 53, 311-316. https://doi.org/10.1111/j.1751-3928.2003.tb00180.x

Moyen, J.F., 2009. High Sr/Y and La/Yb ratios: the meaning of the “adakitic signature”. Lithos, 112, 556-574.

Munkhtsengel, B., Ohara, M., Gerel, O., Dandar, S., Tsuchiya, N., 2007. Preliminary Study of Formation Mechanism of the Erdenetiin Ovoo Porphyry Copper-Molybdenum Deposit and Environmental Effects of Erdenet Mine, Northern Mongolia. In AIP Conference Proceedings, 833, 204-207. American Institute of Physics. https://doi.org/10.1063/1.2207106

Nasdala, L., Hofmeister, W., Norberg, N., Martinson, J.M., Corfu, F., Dörr, W., Kamo, S.L., Kennedy, A.K., Kronz, A., Reiners, P.W. and Frei, D., 2008. Zircon M257-a homogeneous natural reference material for the ion microprobe U-Pb analysis of zircon. Geostandards and Geoanalytical Research, 32, 247-265. https://doi.org/10.1111/j.1751-908X.2008.00914.x

Patchett, P.J., Tatsumoto, M., 1981. A routine high-precision method for Lu-Hf isotope geochemistry and chronology. Contributions to Mineralogy and Petrology, 75, 263-267.

Patiño Douce, A.E., 1997. Generation of metaluminous A-type granites by low-pressure melting of calc-alkaline granitoids. Geology, 25, 743-746.

Pearce, J.A., Harris, N.B. and Tindle, A.G., 1984. Trace element discrimination diagrams for the tectonic interpretation of granitic rocks. Journal of Petrology, 25, 956-983.

Pearce, J.A., Peate, D.W., 1995. Tectonic implications of the composition of volcanic arc magmas. Annual Review of Earth and Planetary Sciences, 23, 251-286.

Pearce, J.A., 2008. Geochemical fingerprinting of oceanic basalts with applications to ophiolite classification and the search for Archean oceanic crust. Lithos, 100, 14-48.

Peccerillo, A., Taylor, S.R., 1976. Geochemistry of Eocene calc-alkaline volcanic rocks from the Kastamonu area, northern Turkey. Contributions to Mineralogy and Petrology, 58, 63-81.

Rubatto, D., Hermann, J., 2003. Zircon formation during fluid circulation in eclogites (Monviso, Western Alps): implications for Zr and Hf budget in subduction zones. Geochimica et Cosmochimica acta, 67, 2173-2187.

Rudnick, R.L., Gao, S., 2003. Composition of the continental crust., in Gao, S., Holland, H.D., Turekian, K.K., The Crust, 3, Elsevier, Amsterdam, Netherlands. pp. 1-64

Safonova, I., Seltmann, R., Kröner, A., Gladkochub, D., Schulmann, K., Xiao, W., Kim, J., Komiya, T., Sun, M., 2011. A new concept of continental construction in the Central Asian Orogenic Belt. Episodes, 34, 186-196.

Safonova, I., Kotlyarov, A., Krivonogov, S., Xiao, W., 2017. Intra-oceanic arcs of the Paleo-Asian Ocean. Gondwana Research, 50, 167-194.

Safonova, I., 2017. Juvenile versus recycled crust in the Central Asian Orogenic Belt: Implications from ocean plate stratigraphy, blueschist belts and intra-oceanic arcs. Gondwana Research, 47, 6-27.

Schmitz, M.D., Vervoort, J.D., Bowring, S.A., Patchett, P.J., 2004. Decoupling of the Lu-Hf and Sm-Nd isotope systems during the evolution of granulitic lower crust beneath southern Africa. Geology, 32, 405-408. https://doi.org/10.1130/G20241.1

Sláma, J., Košler, J., Condon, D.J., Crowley, J.L., Gerdes, A., Hanchar, J.M., Horstwood, M.S., Morris, G.A., Nasdala, L., Norberg, N., Schaltegger, U., 2008. Plešovice zircon–a new natural reference material for

U-Pb and Hf isotopic microanalysis. Chemical Geology, 249, 1-35. https://doi.org/10.1016/j.chemgeo.2007.11.005

Söderlund, U., Patchett, P.J., Vervoort, J.D., Isachsen, C.E., 2004. The 176Lu decay constant determined by Lu-Hf and U-Pb isotope systematics of Precambrian mafic intrusions. Earth and Planetary Science Letters, 219, 311-324. https://doi.org/10.1016/S0012-821X(04)00012-3

Sorokin, A.A., Zaika, V.A., Kovach, V.P., Kotov, A.B., Xu, W., Yang, H., 2020. Timing of closure of the eastern Mongol–Okhotsk Ocean: Constraints from U-Pb and Hf isotopic data of detrital zircons from metasediments along the Dzhagdy Transect. Gondwana Research, 81, 58-78. https://doi.org/10.1016/j.gr.2019.11.009

Sun, S.S., McDonough, W.F., 1989. Chemical and isotopic systematics of oceanic basalts: implications for mantle composition and processes. Geological Society, London, Special Publications, 42, 313-345. https://doi.org/10.1144/GSL.SP.1989.042.01.19

Sun, D.Y., Gou, J., Wang, T.H., Ren, Y.S., Liu, Y.J., Guo, H.Y., Liu, X.M., Hu, Z.C., 2013. Geochronological and geochemical constraints on the Erguna massif basement, NE China–subduction history of the Mongol–Okhotsk oceanic crust. International Geology Review, 55, 1801-1816.

Taylor, S.R., McLennan, S.M., 1995. The geochemical evolution of the continental crust. Reviews of geophysics, 33, 241-265.

Tiepolo, M., Vannucci, R., 2014. The contribution of amphibole from deep arc crust to the silicate Earth's Nb budget. Lithos, 208, 16-20. https://doi.org/10.1016/j.lithos.2014.07.028

Tomurtogoo, O., Windley, B.F., Kröner, A., Badarch, G., Liu, D.Y., 2005. Zircon age and occurrence of the Adaatsag ophiolite and Muron shear zone, central Mongolia: constraints on the evolution of the Mongol–Okhotsk ocean, suture and orogen. Journal of the Geological Society, 162, 125-134. https://doi.org/10.1144/0016-764903-146

Tumurchudur, D., Bold, G., Chuluun, D., Gundsambuu, Ts., 2006. Geological Map of the Ikh-Khorgo area, Scale 1:50,000. Gurvantalst LLC, Mongolia (in Mongolian)

Turner, S.P., Foden, J.D., Morrison, R.S., 1992. Derivation of some A-type magmas by fractionation of basaltic magma: an example from the Padthaway Ridge, South Australia. Lithos, 28, 151-179. https://doi.org/10.1016/0024-4937(92)90029-X

Vermeesch, P., 2018. IsoplotR: A free and open toolbox for geochronology. Geoscience Frontiers, 9(5), 1479-1493. https://doi.org/10.1016/j.gsf.2018.04.001

Vervoort, J.D., Patchett, P.J., Blichert-Toft, J., Albarède, F., 1999. Relationships between Lu-Hf and Sm-Nd isotopic systems in the global sedimentary system. Earth and Planetary Science Letters, 168, 79-99.

Whalen, J.B., Currie, K.L., Chappell, B.W., 1987. A-type granites: geochemical characteristics, discrimination and petrogenesis. Contributions to mineralogy and petrology, 95, 407-419.

Wiedenbeck, M., Hanchar, J.M., Peck, W.H., Sylvester, P., Valley, J., Whitehouse, M., Kronz, A., Morishita, Y., Nasdala, L., Fiebig, J., Franchi, I., 2004. Further characterisation of the 91500 zircon crystal. Geostandards and Geoanalytical Research, 28, 9-39.

Wilhem, C., Windley, B.F., Stampfli, G.M., 2012. The Altaids of Central Asia: a tectonic and evolutionary innovative review. Earth-Science Reviews, 113, 303-341. https://doi.org/10.1016/j.earscirev.2012.04.001

Windley, B.F., Alexeiev, D., Xiao, W., Kröner, A., Badarch, G., 2007. Tectonic models for accretion of the Central Asian Orogenic Belt. Journal of the Geological Society, 164, 31-47. https://doi.org/10.1144/0016-76492006-022

Wu, F.Y., Yang, Y.H., Xie, L.W., Yang, J.H., Xu, P., 2006. Hf isotopic compositions of the standard zircons and baddeleyites used in U-Pb geochronology. Chemical Geology, 234, 105-126. https://doi.org/10.1016/j.chemgeo.2006.05.003

Xiao, W., Huang, B., Han, C., Sun, S., Li, J., 2010. A review of the western part of the Altaids: a key to understanding the architecture of accretionary orogens. Gondwana Research, 18, 253-273.

Yarmolyuk, V.V., Kovalenko, V.I., Sal'nikova, E.B., Budnikov, S.V., Kovach, V.P., Kotov, A.B., Ponomarchuk, V.A., 2002. Tectono-magmatic zoning, magma sources, and geodynamics of the Early Mesozoic Mongolia-Transbaikal province. Geotectonics, 36, 293-311.

Yarmolyuk, V.V., Kuzmin, M.I., Ernst, R.E., 2014. Intraplate geodynamics and magmatism in the evolution of the Central Asian Orogenic Belt. Journal of Asian Earth Sciences, 93, 158-179. https://doi.org/10.1016/j.jseaes.2014.07.004

Yi, Z., Meert, J.G., 2020. A closure of the Mongol-Okhotsk Ocean by the Middle Jurassic: Reconciliation of paleomagnetic and geological evidence. Geophysical Research Letters, 47, https://doi.org/10.1029/2020GL088235

Zhao, P., Xu, B., Jahn, B.M., 2017. The Mongol-Okhotsk Ocean subduction-related Permian peraluminous granites in northeastern Mongolia: Constraints from zircon U-Pb ages, whole-rock elemental and Sr-Nd-Hf isotopic compositions. Journal of Asian Earth Sciences, 144, 225-242. https://doi.org/10.1016/j.jseaes.2017.03.022

Zhu, M., Zhang, F., Miao, L., Baatar, M., Anaad, C., Yang, S., Li, X., 2016. Geochronology and geochemistry of the Triassic bimodal volcanic rocks and coeval A-type granites of the Olzit area, Middle Mongolia: Implications for the tectonic evolution of Mongol–Okhotsk Ocean. Journal of Asian Earth Sciences, 122, 41-57. https://doi.org/10.1016/j.jseaes.2016.03.001

Zhu, M.S., Zhang, F., Miao, L.C., Baatar, M., Anaad, C., Yang, S.H., Li, X.B., 2018. The late Carboniferous khuhu davaa ophiolite in northeastern Mongolia: Implications for the tectonic evolution of the Mongol–Okhotsk ocean. Geological Journal, 53, 1263-1278.

Figure 1

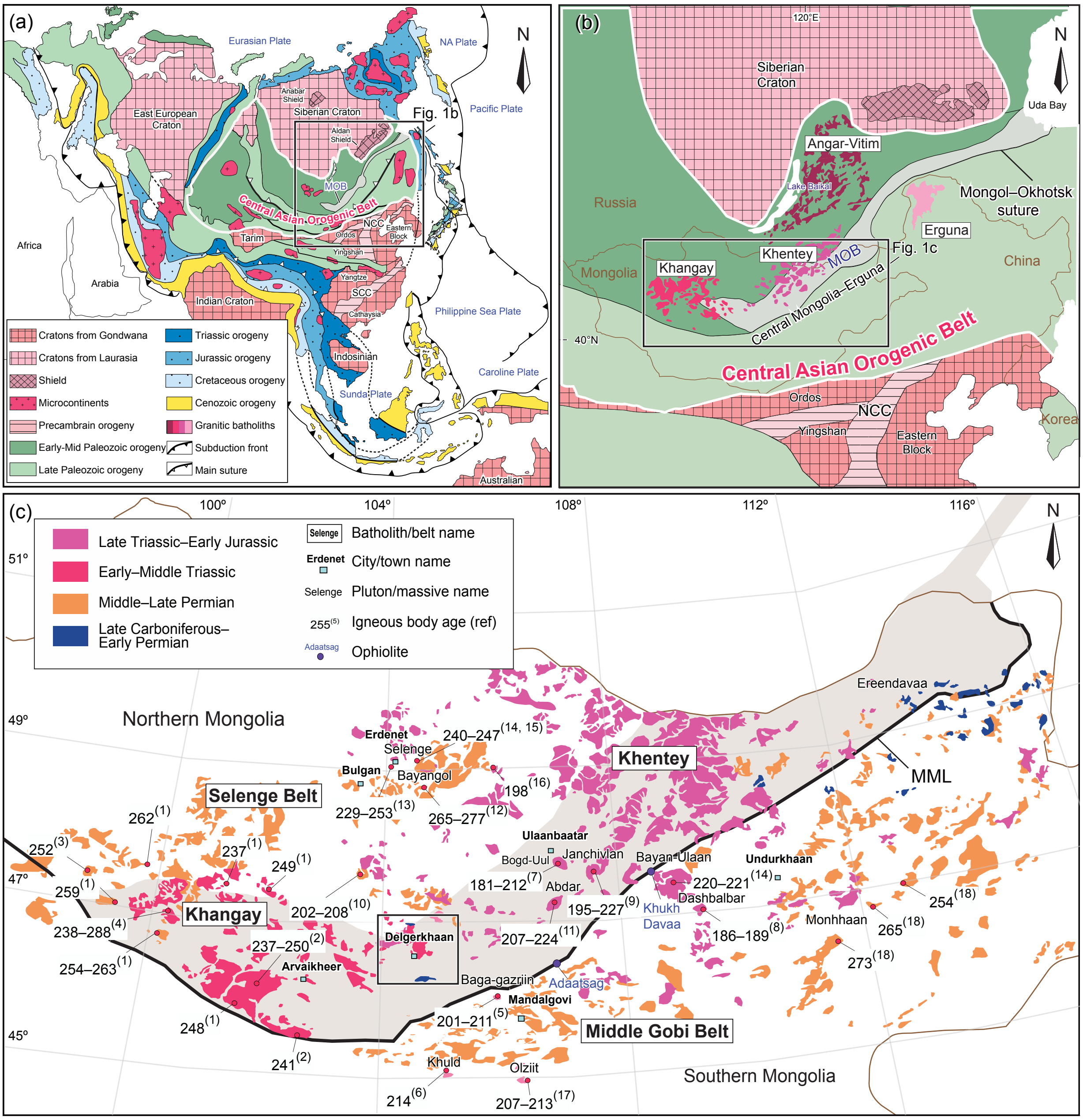

(a)
Eurasian Plate
NA Plate
Pacific Plate
East European Craton
Siberian Craton
Fig. 1b
MOB
Central Asian Orogenic Belt
Tarim
NCC
Africa
Arabia
Indian Craton
Yangtze
SCC
Cathaysia
Philippine Sea Plate
Indosinian
Caroline Plate
Sunda Plate
Australian
Cratons from Gondwana
Cratons from Laurasia
Shield
Microcontinents
Precambrain orogeny
Early-Mid Paleozoic orogeny
Late Paleozoic orogeny
Triassic orogeny
Jurassic orogeny
Cretaceous orogeny
Cenozoic orogeny
Granitic batholiths
Subduction front
Main suture
(b)
120°E
Siberian Craton
Uda Bay
Angar-Vitim
Lake Baikal
Russia
Mongol–Okhotsk suture
Erguna
Fig. 1c
Khangay
Khentey
MOB
Mongolia
China
Central Mongolia–Erguna
40°N
Central Asian Orogenic Belt
Ordos
NCC
Yingshan
Eastern Block
Korea
(c)
100°
104°
108°
112°
116°
N
51°
49°
47°
45°
Late Triassic–Early Jurassic
Early–Middle Triassic
Middle–Late Permian
Late Carboniferous–Early Permian
Batholith/belt name
City/town name
Pluton/massive name
Igneous body age (ref)
Ophiolite
Northern Mongolia
Erdenet
Selenge
Bulgan
Bayangol
240–247(14, 15)
198(16)
229–253(13)
265–277(12)
Khentey
Selenge Belt
262(1)
252(3)
237(1)
249(1)
259(1)
Khangay
238–288(4)
202–208(10)
254–263(1)
237–250(2)
Arvaikheer
Delgerkhaan
Ulaanbaatar
Bogd-Uul
Janchivlan
181–212(7)
Abdar
195–227(9)
207–224(11)
Bayan-Ulaan
220–221(14)
Dashbalbar
Khukh Davaa
186–189(8)
Undurkhaan
Monhhaan
265(18)
254(18)
273(18)
Ereendavaa
MML
Baga-gazriin
Adaatsag
Mandalgovi
201–211(5)
Middle Gobi Belt
248(1)
241(2)
Khuld
214(6)
Olziit
207–213(17)
Southern Mongolia

Figure 2

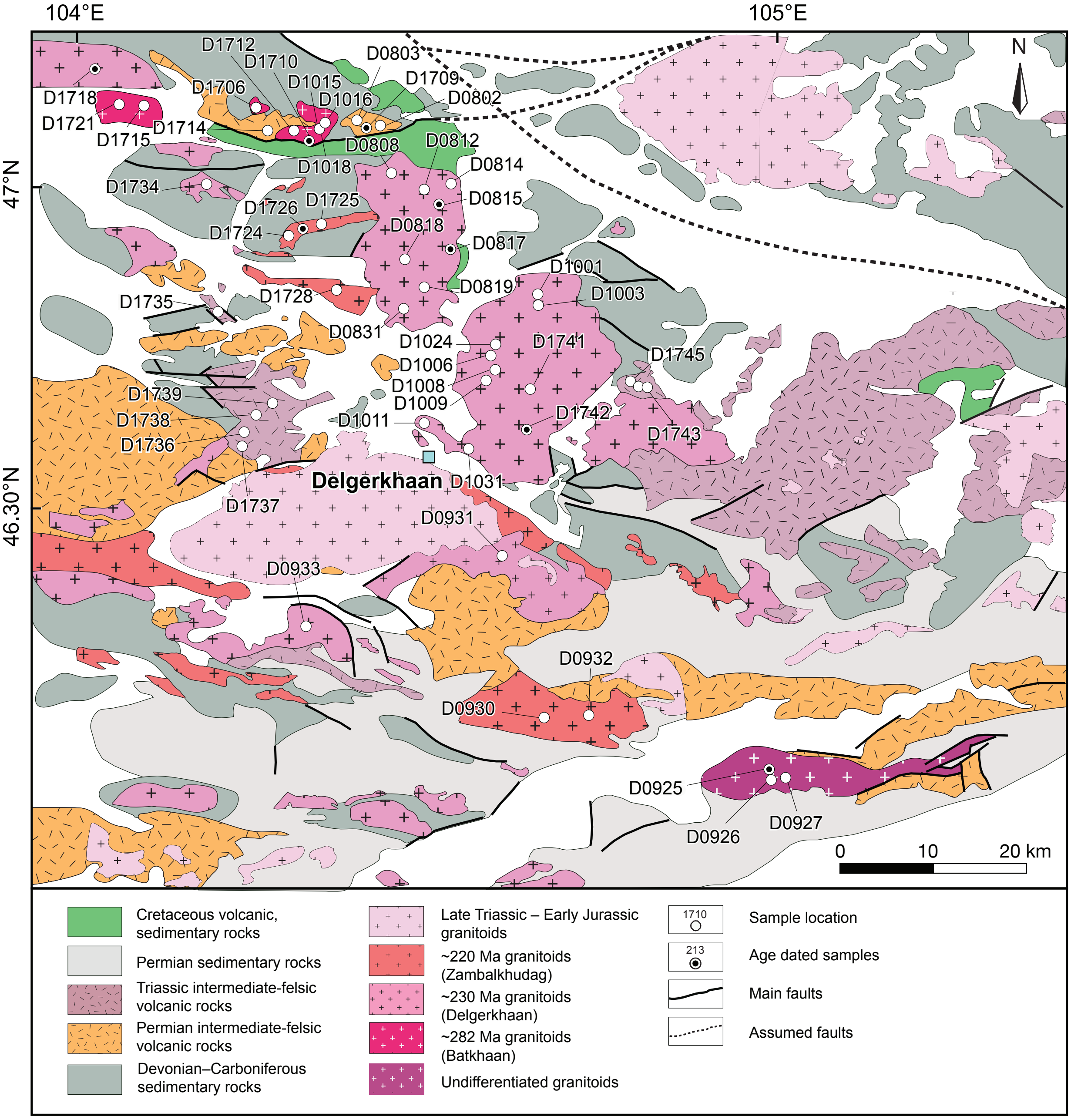

104°E
105°E
47°N
46.30°N
N
Delgerkhaan
D1712
D1710
D0803
D1709
D1015
D1016
D0802
D1706
D1718
D1721
D1714
D1715
D0808
D0812
D1018
D0814
D1734
D0815
D1726
D1725
D0818
D1724
D0817
D1001
D1735
D1728
D0819
D1003
D0831
D1024
D1741
D1745
D1006
D1008
D1009
D1739
D1738
D1011
D1742
D1743
D1736
D1031
D1737
D0931
D0933
D0932
D0930
D0925
D0926
D0927
0
10
20 km
Cretaceous volcanic, sedimentary rocks
Permian sedimentary rocks
Triassic intermediate-felsic volcanic rocks
Permian intermediate-felsic volcanic rocks
Devonian–Carboniferous sedimentary rocks
Late Triassic – Early Jurassic granitoids
~220 Ma granitoids (Zambalkhudag)
~230 Ma granitoids (Delgerkhaan)
~282 Ma granitoids (Batkhaan)
Undifferentiated granitoids
1710
Sample location
213
Age dated samples
Main faults
Assumed faults

Figure 3

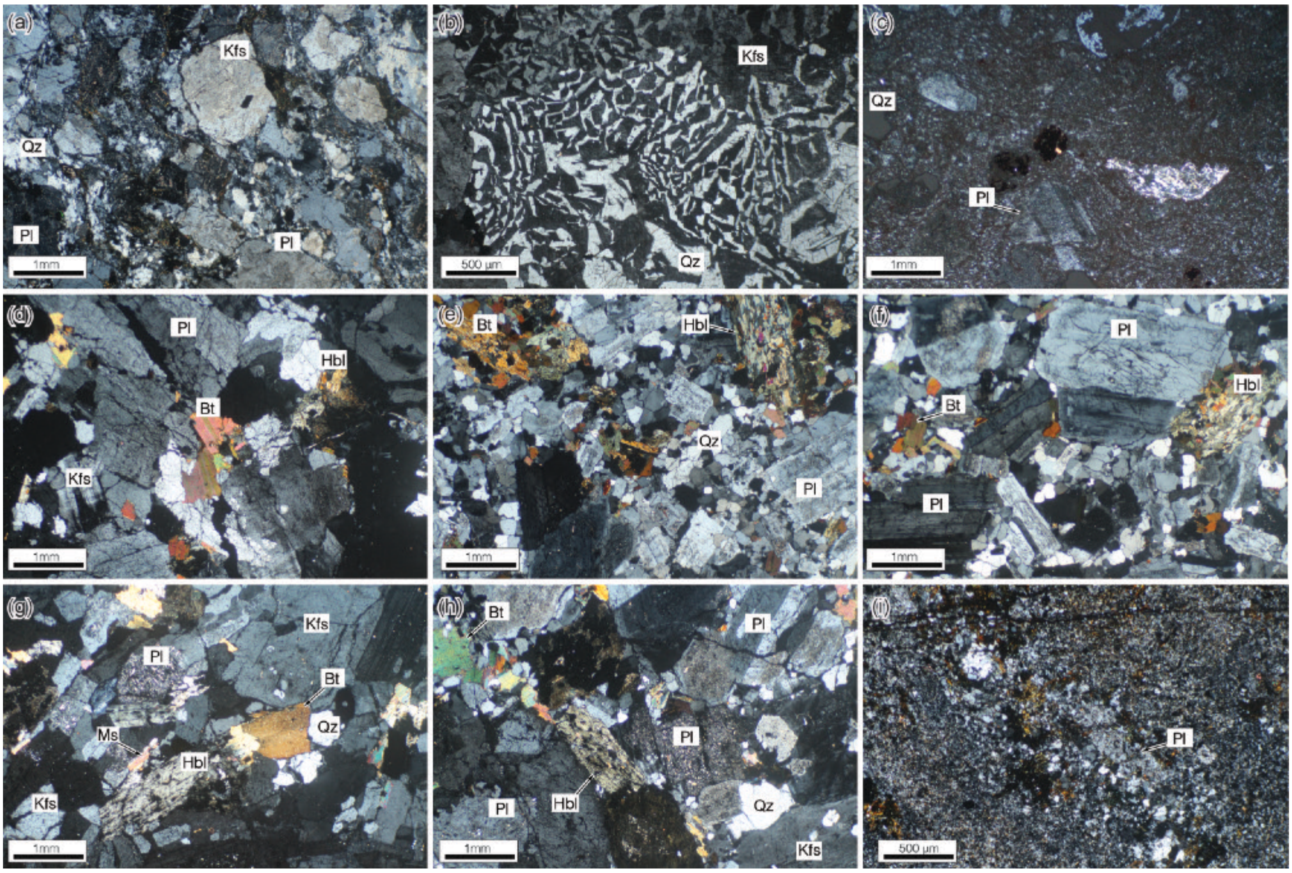

(a)
Kfs
Qz
Pl
Pl
1mm
(b)
Kfs
Qz
500 µm
(c)
Qz
Pl
1mm
(d)
Pl
Hbl
Bt
Kfs
1mm
(e)
Bt
Hbl
Qz
Pl
1mm
(f)
Pl
Hbl
Bt
Pl
1mm
(g)
Kfs
Pl
Bt
Qz
Ms
Hbl
Kfs
1mm
(h)
Bt
Pl
Pl
Pl
Hbl
Qz
Kfs
1mm
(i)
Pl
500 µm

Figure 4

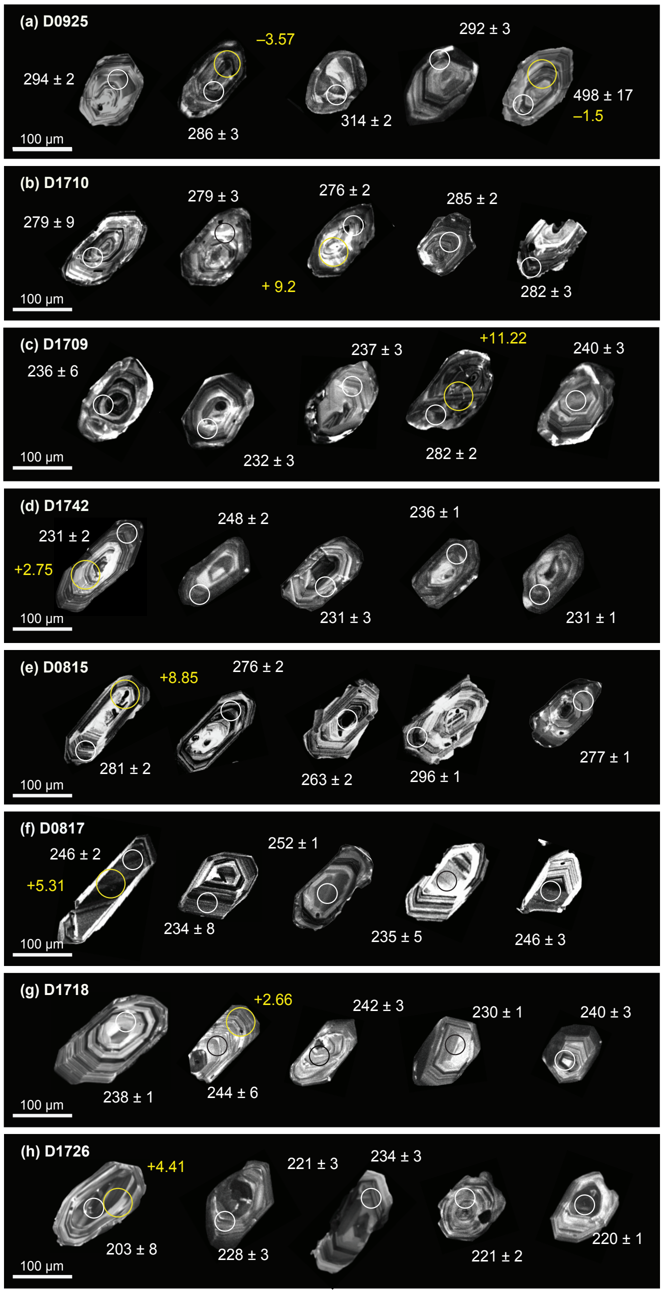
(a) D0925
294 ± 2
−3.57
286 ± 3
314 ± 2
292 ± 3
498 ± 17
−1.5
100 μm
(b) D1710
279 ± 9
279 ± 3
276 ± 2
+ 9.2
285 ± 2
282 ± 3
100 μm
(c) D1709
236 ± 6
232 ± 3
237 ± 3
+11.22
282 ± 2
240 ± 3
100 μm
(d) D1742
231 ± 2
+2.75
248 ± 2
231 ± 3
236 ± 1
231 ± 1
100 μm
(e) D0815
+8.85
276 ± 2
281 ± 2
263 ± 2
296 ± 1
277 ± 1
100 μm
(f) D0817
246 ± 2
+5.31
234 ± 8
252 ± 1
235 ± 5
246 ± 3
100 μm
(g) D1718
238 ± 1
+2.66
244 ± 6
242 ± 3
230 ± 1
240 ± 3
100 μm
(h) D1726
+4.41
203 ± 8
228 ± 3
221 ± 3
234 ± 3
221 ± 2
220 ± 1
100 μm

Figure 5

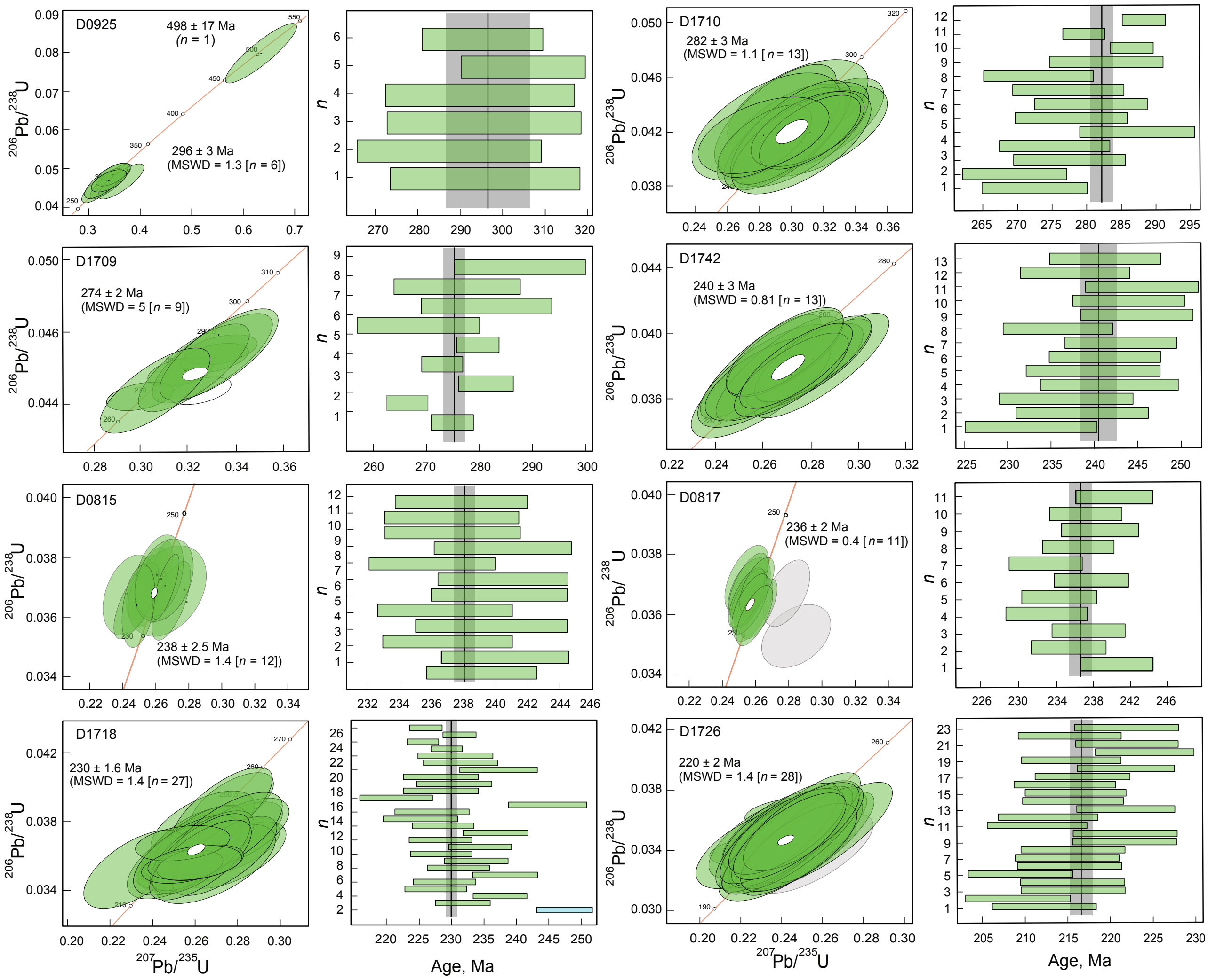

D0925
498 ± 17 Ma
(n = 1)
296 ± 3 Ma
(MSWD = 1.3 [n = 6])
D1710
282 ± 3 Ma
(MSWD = 1.1 [n = 13])
D1709
274 ± 2 Ma
(MSWD = 5 [n = 9])
D1742
240 ± 3 Ma
(MSWD = 0.81 [n = 13])
D0815
238 ± 2.5 Ma
(MSWD = 1.4 [n = 12])
D0817
236 ± 2 Ma
(MSWD = 0.4 [n= 11])
D1718
230 ± 1.6 Ma
(MSWD = 1.4 [n = 27])
D1726
220 ± 2 Ma
(MSWD = 1.4 [n = 28])
206Pb/238U
207Pb/235U
n
Age, Ma

Figure 6

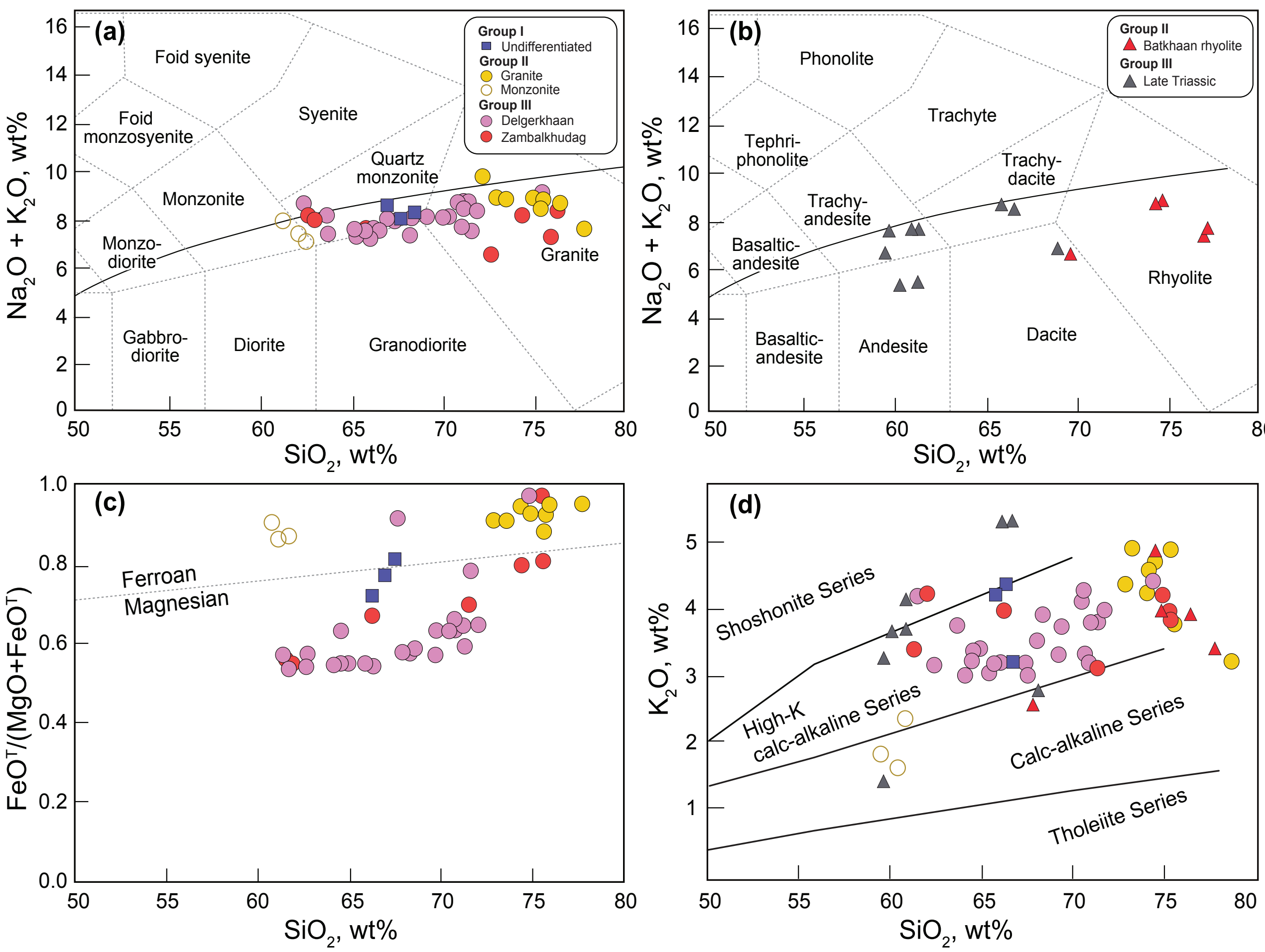
(a)
Group I
Undifferentiated
Group II
Granite
Monzonite
Group III
Delgerkhaan
Zambalkhudag
Foid syenite
Foid monzosyenite
Syenite
Quartz monzonite
Monzonite
Monzo-diorite
Gabbro-diorite
Diorite
Granodiorite
Granite
$Na_2O + K_2O$, wt%
SiO_2, wt%
(b)
Group II
Batkhaan rhyolite
Group III
Late Triassic
Phonolite
Trachyte
Tephri-phonolite
Trachy-dacite
Trachy-andesite
Basaltic-andesite
Basaltic-andesite
Andesite
Dacite
Rhyolite
$Na_2O + K_2O$, wt%
SiO_2, wt%
(c)
Ferroan
Magnesian
$FeO^T/(MgO+FeO^T)$
SiO_2, wt%
(d)
Shoshonite Series
High-K calc-alkaline Series
Calc-alkaline Series
Tholeiite Series
K_2O, wt%
SiO_2, wt%

Figure 7

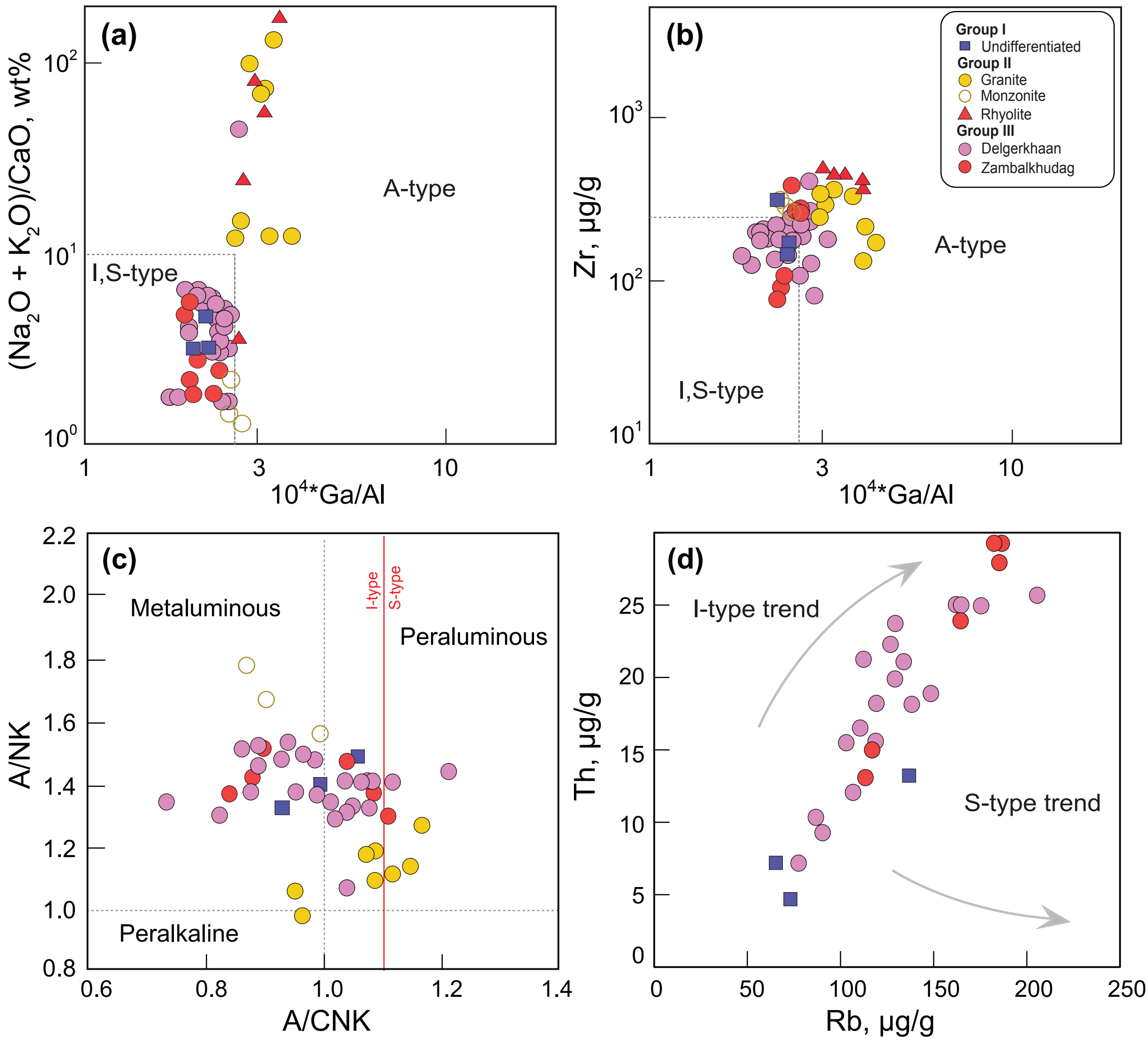

(a)
A-type
I,S-type
10^2
10^1
10^0
$(Na_2O + K_2O)/CaO$, wt%
1
3
10
10^4*Ga/Al
(b)
Group I
Undifferentiated
Group II
Granite
Monzonite
Rhyolite
Group III
Delgerkhaan
Zambalkhudag
A-type
I,S-type
10^3
10^2
10^1
Zr, μg/g
1
3
10
10^4*Ga/Al
(c)
Metaluminous
Peraluminous
Peralkaline
I-type
S-type
2.2
2.0
1.8
1.6
1.4
1.2
1.0
0.8
A/NK
0.6
0.8
1.0
1.2
1.4
A/CNK
(d)
I-type trend
S-type trend
25
20
15
10
5
0
Th, μg/g
0
50
100
150
200
250
Rb, μg/g

Figure 8

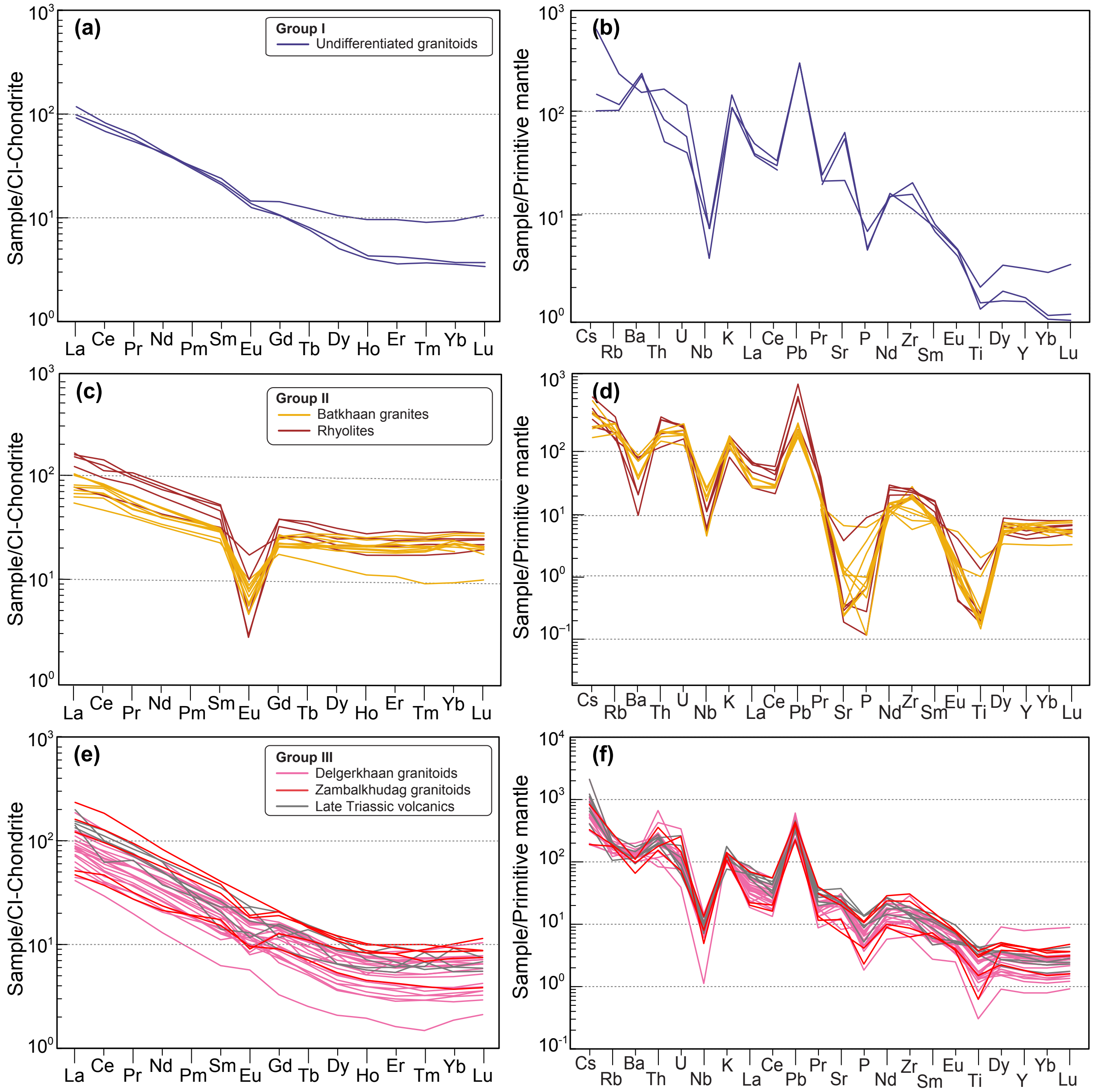
(a)
Group I
Undifferentiated granitoids
Sample/CI-Chondrite
La Ce Pr Nd Pm Sm Eu Gd Tb Dy Ho Er Tm Yb Lu
(b)
Sample/Primitive mantle
Cs Rb Ba Th U Nb K La Ce Pb Pr Sr P Nd Zr Sm Eu Ti Dy Y Yb Lu
(c)
Group II
Batkhaan granites
Rhyolites
Sample/CI-Chondrite
La Ce Pr Nd Pm Sm Eu Gd Tb Dy Ho Er Tm Yb Lu
(d)
Sample/Primitive mantle
Cs Rb Ba Th U Nb K La Ce Pb Pr Sr P Nd Zr Sm Eu Ti Dy Y Yb Lu
(e)
Group III
Delgerkhaan granitoids
Zambalkhudag granitoids
Late Triassic volcanics
Sample/CI-Chondrite
La Ce Pr Nd Pm Sm Eu Gd Tb Dy Ho Er Tm Yb Lu
(f)
Sample/Primitive mantle
Cs Rb Ba Th U Nb K La Ce Pb Pr Sr P Nd Zr Sm Eu Ti Dy Y Yb Lu

Figure 9

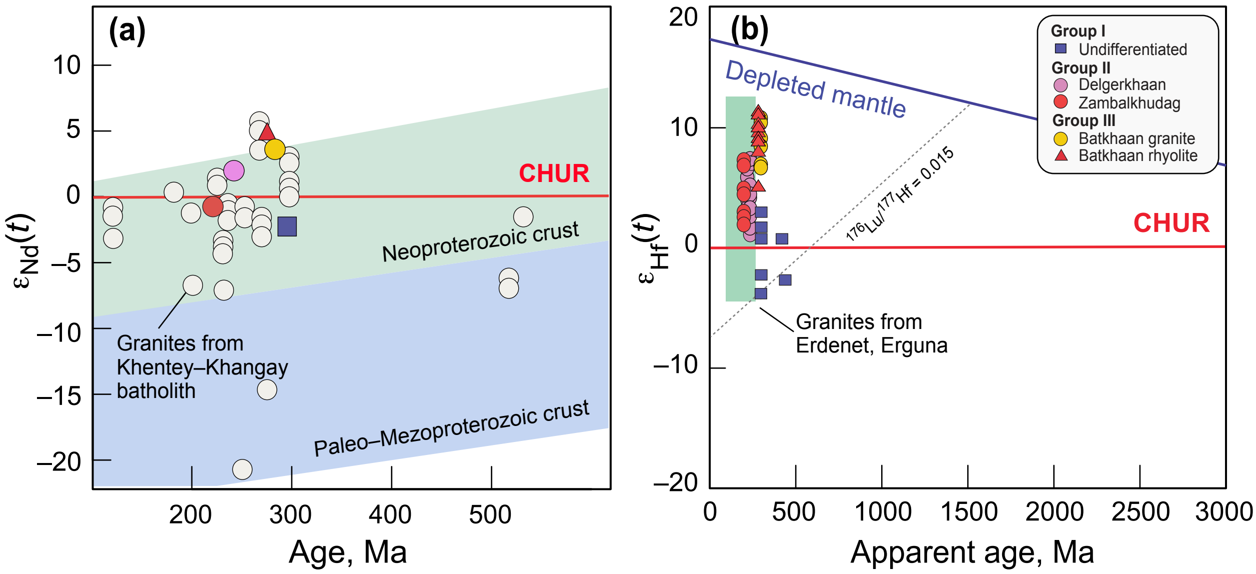

(a)
10
5
0
–5
–10
–15
–20
CHUR
Neoproterozoic crust
Granites from
Khentey–Khangay
batholith
Paleo–Mezoproterozoic crust
200
300
400
500
Age, Ma
$\varepsilon_{Nd}(t)$
(b)
20
10
0
–10
–20
Depleted mantle
$^{176}Lu/^{177}Hf = 0.015$
CHUR
Granites from
Erdenet, Erguna
Group I
Undifferentiated
Group II
Delgerkhaan
Zambalkhudag
Group III
Batkhaan granite
Batkhaan rhyolite
0
500
1000
1500
2000
2500
3000
Apparent age, Ma
$\varepsilon_{Hf}(t)$

Figure 10

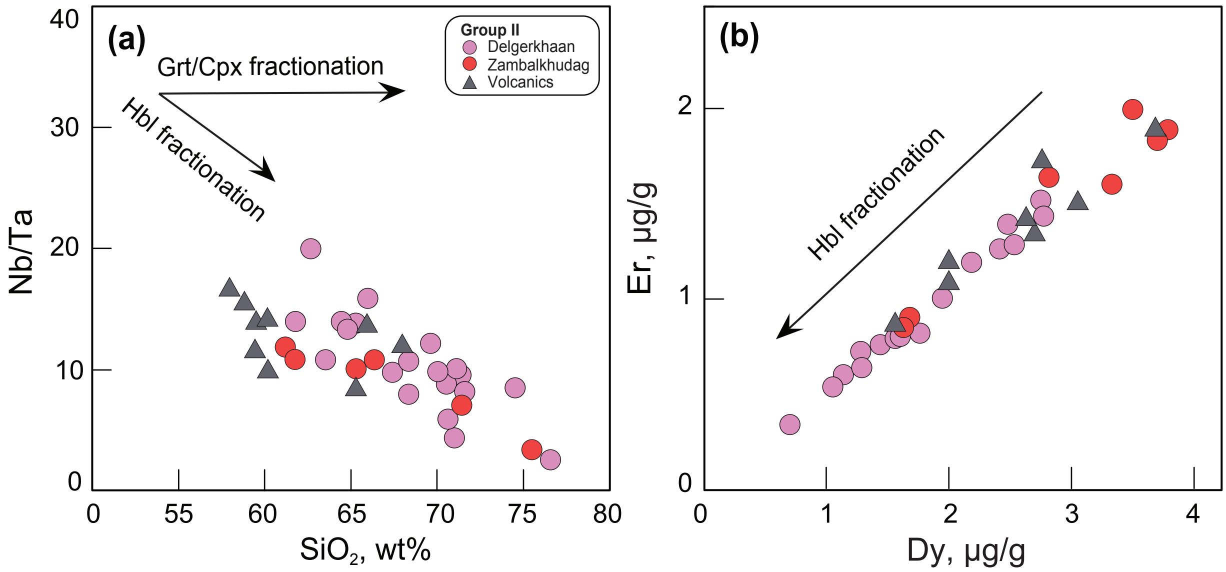

(a)
Grt/Cpx fractionation
Hbl fractionation
Group II
Delgerkhaan
Zambalkhudag
Volcanics
Nb/Ta
40
30
20
10
0
0
55
60
65
70
75
80
SiO2, wt%
(b)
Hbl fractionation
Er, µg/g
2
1
0
0
1
2
3
4
Dy, µg/g

Figure 11

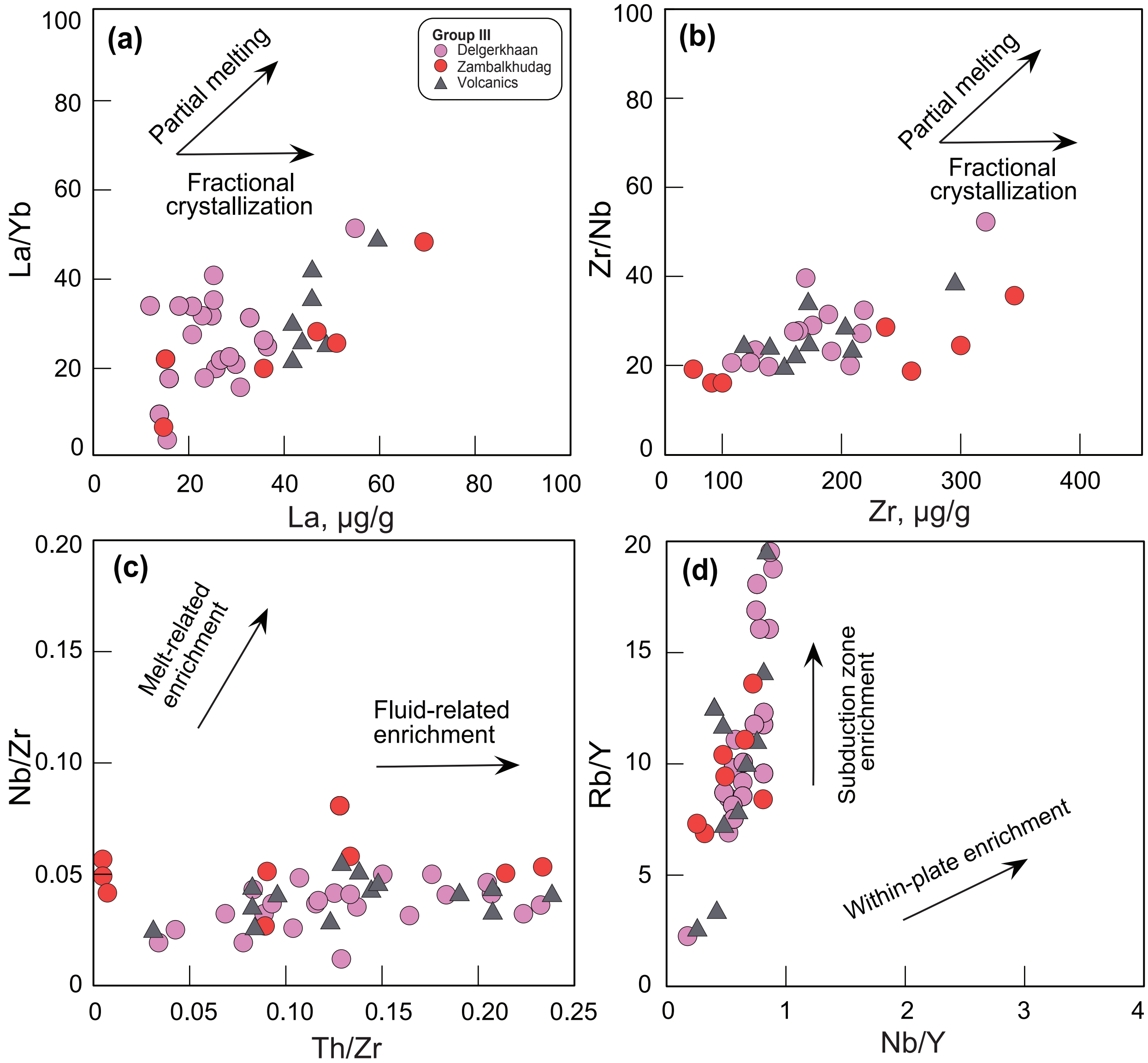
(a)
Group III
Delgerkhaan
Zambalkhudag
Volcanics
Partial melting
Fractional crystallization
La/Yb
La, μg/g
(b)
Partial melting
Fractional crystallization
Zr/Nb
Zr, μg/g
(c)
Melt-related enrichment
Fluid-related enrichment
Nb/Zr
Th/Zr
(d)
Subduction zone enrichment
Within-plate enrichment
Rb/Y
Nb/Y

Figure 12

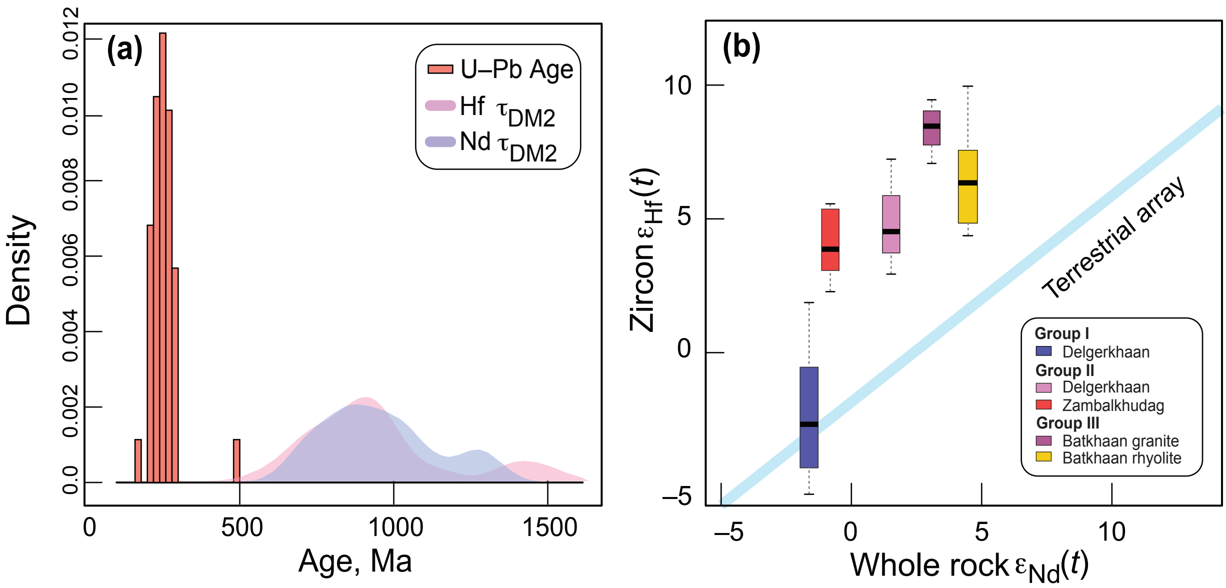

(a)
U–Pb Age
Hf τ_{DM2}
Nd τ_{DM2}
Density
0.0
0.002
0.004
0.006
0.008
0.010
0.012
0
500
1000
1500
Age, Ma
(b)
Terrestrial array
Group I
Delgerkhaan
Group II
Delgerkhaan
Zambalkhudag
Group III
Batkhaan granite
Batkhaan rhyolite
Zircon $\varepsilon_{Hf}(t)$
10
5
0
–5
–5
0
5
10
Whole rock $\varepsilon_{Nd}(t)$

Figure 13

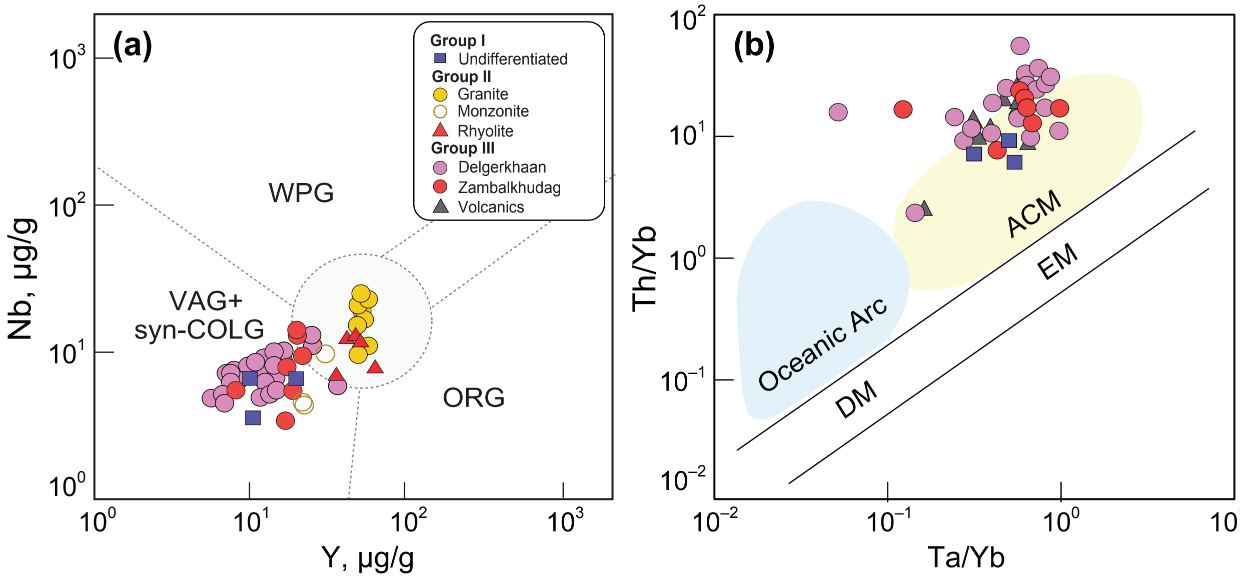

(a)
Group I
Undifferentiated
Group II
Granite
Monzonite
Rhyolite
Group III
Delgerkhaan
Zambalkhudag
Volcanics
WPG
VAG+
syn-COLG
ORG
Nb, µg/g
Y, µg/g
10^0
10^1
10^2
10^3
(b)
Oceanic Arc
ACM
DM
EM
Th/Yb
Ta/Yb
10^{-2}
10^{-1}
10^0
10^1
10^2

Figure 14

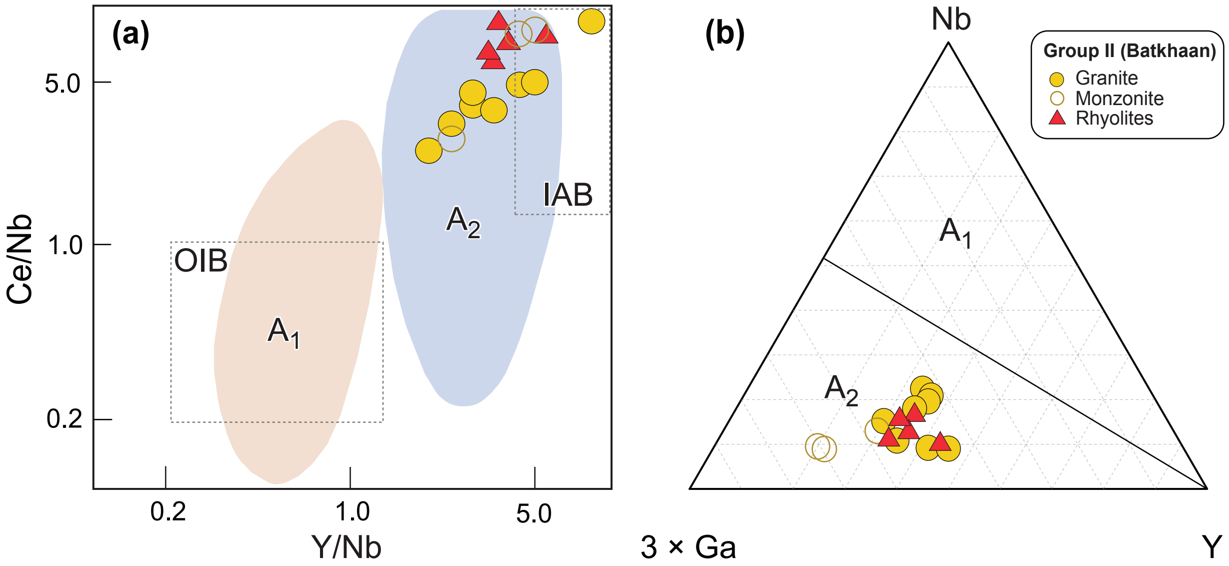

(a)
5.0
1.0
0.2
Ce/Nb
0.2
1.0
5.0
Y/Nb
OIB
A1
A2
IAB
(b)
Nb
Group II (Batkhaan)
Granite
Monzonite
Rhyolites
A1
A2
3 × Ga
Y